

# SILCC – VIII: The impact of far-ultraviolet radiation on star formation and the interstellar medium

Tim-Eric Rathjen,<sup>1,2\*</sup> Stefanie Walch,<sup>1</sup> Thorsten Naab,<sup>2</sup> Pierre Nürnbergger,<sup>1</sup> Richard Wunsch,<sup>3</sup>  
Daniel Seifried,<sup>1</sup> & Simon C. O. Glover<sup>4</sup>

<sup>1</sup>*I. Physikalisches Institut, Universität zu Köln, Zùlpicher Str. 77, 50937 Köln, Germany*

<sup>2</sup>*Max Planck Institute for Astrophysics, Karl-Schwarzschild-Str. 1, 85748 Garching, Germany*

<sup>3</sup>*Astronomical Institute of the Czech Academy of Sciences, Boční II 1401, 141 00 Prague, Czech Republic*

<sup>4</sup>*Zentrum für Astronomie, Institut für Theoretische Astrophysik, Universität Heidelberg, Albert-Ueberle-Str. 2, 69120 Heidelberg, Germany*

Accepted XXX. Received YYY; in original form ZZZ

## ABSTRACT

We present magnetohydrodynamic simulations of star formation in the multiphase interstellar medium to quantify the impact of non-ionising far-ultraviolet (FUV) radiation. This study is carried out within the framework of the SILCC PROJECT. It incorporates the radiative transfer of ionising radiation and self-consistent modelling of variable FUV radiation from star clusters. Near young star clusters, the interstellar radiation field (ISRF) can reach values of  $G_0 \approx 10^4$  (in Habing units), far exceeding the canonical solar neighbourhood value of  $G_0 = 1.7$ . However, our findings suggest that FUV radiation has minimal impact on the integrated star formation rate compared to other feedback mechanisms such as ionising radiation, stellar winds, and supernovae. Only a slight decrease in star formation burstiness, related to increased photoelectric heating efficiency by the variable FUV radiation field, is detectable. Dust near star-forming regions can be heated up to 60 K via the photoelectric (PE) effect, showing a broad temperature distribution. PE heating rates for variable FUV radiation models show higher peak intensities but lower average heating rates than static ISRF models. Simulations of solar neighbourhood conditions without stellar winds or ionising radiation but with self-consistent ISRF and supernovae show high star formation rates  $\sim 10^{-1} M_\odot \text{ yr}^{-1} \text{ kpc}^{-2}$ , contradicting expectations. Our chemical analysis reveals increased cold neutral medium volume-filling factors (VFF) outside the vicinity of stellar clusters with a variable ISRF. Simultaneously, the thermally unstable gas is reduced, and a sharper separation of warm and cold gas phases is observed. The variable FUV field also promotes a diffuse molecular gas phase with VFF of  $\sim 5 - 10$  per cent.

**Key words:** methods: numerical – MHD – radiative transfer – stars: formation – ISM: abundances – galaxies: ISM

## 1 INTRODUCTION

The interstellar medium (ISM) hosts various gas phases that interact dynamically and chemically, playing a key role in star formation and galaxy evolution (Wolfire et al. 1995; Ferrière 2001; Naab & Ostriker 2017, and references therein). Understanding these interactions is crucial for advancing our knowledge of how galaxies form and evolve.

Star formation occurs in the cold neutral medium (CNM), characterised by its high gas densities and efficient shielding from the interstellar radiation field (ISRF). Stellar feedback mechanisms in the form of ionising radiation, stellar winds, and supernova (SN) explosions, have a significant impact on the ISM, driving turbulence, shaping its morphology, and regulating the star formation activity (Girichidis et al. 2020; Schinnerer & Leroy 2024, and references therein). However, the relative importance of various stellar feedback mechanisms and their implications for star formation are not yet conclusively understood. Ionising radiation and winds from massive O- and B-type stars are thought to regulate or even halt further

gas accretion onto newly formed stellar associations and modify the properties of the ambient gas before the onset of SNe. This early stellar feedback might take precedence over the aforementioned cataclysmic events at the end of a massive star’s lifetime (see e.g. Walch et al. 2012; Gatto et al. 2017; Haid et al. 2019; Rathjen et al. 2021).

Among the early feedback processes, ionising ultraviolet radiation (EUV,  $E_\gamma > 13.6 \text{ eV}$ ) was suggested to be the main agent for dispersing natal molecular clouds. This process regulates the local star formation rate (SFR) by drastically reducing gas accretion onto protostars and star clusters while creating HII regions (see e.g. McKee 1989; Ali & Harries 2019; Rathjen et al. 2021). The ionised gas within HII regions is mostly optically thin for the non-ionising far-ultraviolet (FUV,  $E_\gamma = 5.6 - 13.6 \text{ eV}$ ) radiation emitted by star clusters. This radiation is notable for its ability to dissociate molecular hydrogen (Lyman-Werner band photons) and directly heats the ambient gas via photoelectric (PE) heating on dust grains. These processes influence the chemical composition and physical properties of the surrounding gas, especially in photodissociation regions (PDRs) (see e.g. Draine 1978; Wolfire et al. 1995; Hollenbach & Tielens 1999). It has been suggested that PE heating could explain the ther-

\* E-mail: rathjen@ph1.uni-koeln.de

mal pressure in the diffuse gas and set the global SFR of galactic discs in dynamical and thermal equilibrium (see e.g. [Ostriker et al. 2010](#); [Kim et al. 2011](#)). In regions sufficiently shielded from EUV and FUV light, low-energy cosmic rays (CRs) are the main agents of  $\text{H}_2$  ionisation and the resulting heating ([Bakes & Tielens 1994](#)). Together, the strength of the UV radiation field and the low-energy CR ionisation rate,  $\zeta_{\text{CR}}$ , control the thermal and chemical state of the warm neutral medium (WNM) and the CNM ([Wolfire et al. 2003](#)). Stars are sources of the UV radiation field, which therefore varies in space and time. Hence, an assumed constant ISRF based on estimates and local observations (e.g. [Draine 1978](#)) might be insufficient to describe the state of the ISM properly.

Observations ([Calzetti et al. 2000](#); [Leroy et al. 2008](#); [Ossenkopf et al. 2013](#)) and theoretical models ([Röllig et al. 2007](#); [Bisbas et al. 2021](#); [Pound & Wolfire 2023](#)) of nearby star-forming regions have provided valuable insights into the effects of FUV radiation on the ISM. These studies have demonstrated the presence and structure of PDRs, where FUV radiation from young stellar clusters interacts with surrounding molecular clouds, influencing the chemical and physical properties of neutral gas layers (see e.g. [Hollenbach & Tielens 1999](#), for a review). Additionally, observations have revealed specific FUV-driven processes such as photodissociation of molecules, heating of neutral gas, and the formation of particular molecular species characteristic of PDRs. Theoretical models and numerical simulations at various scales have supplemented these observations and have further studied the influence of FUV radiation on the ISM and its star-forming properties (e.g. [Kim & Ostriker 2017](#); [Hill et al. 2018](#); [Bialy 2020](#)). On the star cluster scale, [Ali & Harries \(2019\)](#) have studied how the varying FUV radiation fields in simulated massive star clusters affect the photoevaporation of protoplanetary discs near massive stars. ISM simulations of galactic patches have included the relevant physical processes to study the impact of stellar feedback on the cold gas phase (e.g. [Butler et al. 2017](#); [Rathjen et al. 2021](#); [Hu et al. 2022](#); [Rathjen et al. 2023](#); [Kim et al. 2023b](#)). Recently, numerical advances have made it possible to simulate isolated (dwarf) galaxies with adequate resolution to capture the major physical processes and explicit star formation and feedback (e.g. [Forbes et al. 2016](#); [Hu et al. 2017](#); [Emerick et al. 2018](#); [Lahén et al. 2019](#); [Agertz et al. 2020](#); [Tress et al. 2020](#); [Andersson et al. 2024](#); [Fotopoulou et al. 2024](#)). However, individual studies incorporate different physical processes and combinations of stellar feedback mechanisms with different numerical resolutions. Among other uncertainties, the relative importance of FUV radiation compared to other stellar feedback mechanisms and its impact on the global characteristics of the ISM remains to be clarified.

In this study, we comprehensively investigate the effects of variable (in space and time) FUV radiation on the SFR and the chemical composition of the multiphase ISM in a stratified galactic patch, utilising magnetohydrodynamic (MHD) simulations conducted within the SILCC PROJECT ([Walch et al. 2015](#); [Girichidis et al. 2016](#); [Gatto et al. 2017](#); [Peters et al. 2017](#); [Girichidis et al. 2018b](#); [Rathjen et al. 2021](#); [Rathjen et al. 2023](#)). Our new simulations incorporate a self-consistent modelling of the ISRF, allowing us to explore the local variations in the FUV intensity and its effects on the surrounding ISM.

This paper is organised as follows: In Sect. 2, we provide an overview of the SILCC PROJECT simulation framework and our methodology to incorporate FUV radiation (Sect. 2.1) and resulting theoretical predictions (Sect. 2.2). We present our simulation results in Sect. 3, focusing on the influence of FUV radiation on the SFR (Sect. 3.1) and the chemical properties of the ISM (Sect. 3.2 - 3.4). In Sect. 4, we discuss the implications of our findings and

compare them to the existing literature. The caveats of our models are assessed in Sect. 4.3. We conclude the study in Sect. 5. To ensure the flow of reading, we include additional material in the Appendix. Appendix A presents a tabulated summary of our main findings. We study the free parameters of our new ISRF model in Appendix B and detail how the ISRF affects our chemical network in Appendix C. We furthermore complement the analysis presented in the main body of the text in Appendices D, E and F.

## 2 NUMERICAL METHODS

This work expands upon [Rathjen et al. \(2023\)](#) and employs the same parameters and methods unless otherwise stated. The new method developed to treat the variable FUV field is described in detail. All other numerical methods are briefly summarised in the following.

We simulate the evolution of the multiphase ISM with the adaptive mesh refinement (AMR) code FLASH v4.6.2 ([Fryxell et al. 2000](#)). We solve the MHD equations using a modified three-wave solver based on [Bouchut et al. \(2007\)](#) and [Waagan et al. \(2011\)](#). Multiple modules are included to model a variety of physical processes such as:

(i) a chemical network based on [Nelson & Langer \(1997\)](#); [Glover & Mac Low \(2007\)](#) to follow the abundances of seven species (atomic (H), molecular ( $\text{H}_2$ ), and ionised ( $\text{H}^+$ ) hydrogen, carbon monoxide (CO) and ionised carbon ( $\text{C}^+$ ), atomic oxygen (O), and free electrons ( $e^-$ )) and to treat the gas heating, cooling, and molecule formation (see [Walch et al. 2015](#), for details);

(ii) gravity due to an external stellar potential and self-gravity evaluated with an Octree-based method ([Wünsch et al. 2018](#));

(iii) CRs, which are being injected in the shocks of SN remnants with an efficiency of 10 per cent (i.e.  $E_{\text{CR}} = 0.1 \times E_{\text{SN}} = 10^{50}$  erg). They are modelled as an additional relativistic fluid with a non-isotropic advection-diffusion scheme ([Girichidis et al. 2018a](#)). This fluid adds CR pressure,  $P_{\text{CR}}$ , and CR energy density,  $u_{\text{CR}}$  terms to the MHD equations. We account for adiabatic cooling and hadronic cooling losses (see [Girichidis et al. 2018a](#); [Rathjen et al. 2021](#); [Rathjen et al. 2023](#), for details);

(iv) star formation of individual massive stars. The stars are tracked with a subgrid model for sink particles that represent star clusters ([Gatto et al. 2017](#)) with a sink particle accretion radius of  $r_{\text{accr}} = 3\Delta x \approx 12$  pc and an accretion threshold density of  $\rho_{\text{thr}} = 2.1 \times 10^{-21}$  g cm $^{-3}$ . The N-body dynamics of the sink particles is integrated with a fourth-order Hermite integrator ([Dinbbier & Walch 2020](#));

(v) stellar feedback from massive stars in the form of supernovae ([Gatto et al. 2015](#)), stellar winds ([Gatto et al. 2017](#)), and ionising (EUV) radiation ([Peters et al. 2017](#); [Haid et al. 2018](#); [Rathjen et al. 2021](#)) that is treated with the backward ray-tracing scheme TREERAY ([Wünsch et al. 2021](#)).

In all previous SILCC PROJECT publications, the ISRF was set to a constant value that got attenuated using the TREERAY/OPTICALDEPTH algorithm ([Wünsch et al. 2018](#)), which follows the same principle idea as the TREECOL algorithm developed by [Clark et al. \(2012\)](#). For each grid cell in the computational domain, the TREERAY/OPTICALDEPTH module computes the column densities of total gas,  $\text{H}_2$ , and CO using a HEALPIX tessellation of the unit sphere with  $n_{\text{rays}} = 48$  directions. It then computes 3D averages and stores these quantities.

For example, the local  $A_{V,3D}$  is:

$$A_{V,3D} = -\frac{1}{2.5} \ln \left[ \frac{1}{n_{\text{rays}}} \sum_{\text{ray}=1}^{n_{\text{rays}}} \exp \left( -2.5 \frac{N_{H,\text{ray}}}{1.87 \times 10^{21} \text{cm}^{-2}} \right) \right], \quad (1)$$

where  $N_{H,\text{ray}}$  is the total gas column density along each direction. The  $A_{V,3D}$  is used to attenuate the ISRF. The columns of  $\text{H}_2$  and  $\text{CO}$  are subsequently used to calculate the amount of (self-)shielding of these species, and the total gas column is used to compute the dust attenuation within the chemistry network (see [Walch et al. 2015](#)).

The FUV ISRF is typically measured in Habing units:

$$G_0 = \frac{u_{\text{FUV}}}{5.29 \times 10^{-14} \text{erg cm}^{-3}}, \quad (2)$$

with the energy density,  $u_{\text{FUV}}$ , in the FUV photon energy range between 5.6 and 13.6 eV. In these units, the standard ISRF in the solar neighbourhood has been estimated as  $G_0 = 1.7$  ([Draine 1978](#)). For studies of different galactic environments presented in [Rathjen et al. \(2023\)](#), the ISRF has been scaled with the gas surface density in a way that it increases linearly with the typical SFR predicted by [Kennicutt \(1998\)](#).

In this study, we assume a lower background ISRF of  $G_{\text{bg}} = 0.0948$ . This value is derived for a cosmic UV background taken from [Haardt & Madau \(2012\)](#) plus an assumed static, preexisting, low-mass stellar population with a stellar surface density of  $\Sigma_{\star} = 30 \text{M}_{\odot} \text{pc}^{-2}$ . We include a model for an old stellar population to account for the gravitational potential of those stars. The old stellar population is assumed to be at solar metallicity and does not evolve in time. Those stars do not exert any feedback in our model and are not tracked.

This paper extends the stellar feedback model to consider the additional FUV radiation from all formed star cluster sink particles. Sect. 2.1 describes how the star cluster FUV luminosity is calculated. In any case, the FUV field from a star or star cluster, like any other radiation field, is diluted as a function of the radial distance  $R$  from the source according to the standard inverse square law,

$$G_{\text{clus}}(R) \propto R^{-2}. \quad (3)$$

Together with the background, the local unattenuated strength of the ISRF is

$$G_0 = \left( \sum_{N_{\text{cluster}}} G_{\text{clus}} \right) + G_{\text{bg}}. \quad (4)$$

Additionally, dust effectively absorbs the FUV light. Hence, the spatially varying FUV radiation field of all star clusters as well as  $G_{\text{bg}}$  must be attenuated. The local dust attenuation is computed in every grid cell using the `TREERAY/OPTICALDEPTH` module ([Wünsch et al. 2018](#)). From each cell in the computational domain, the distance over which the local attenuation, i.e. the visual extinction  $A_{V,3D}$ , is computed is limited to  $d = 50 \text{pc}$ , which is the typical distance between massive stars in the solar neighbourhood. For the effective strength of the local dust-attenuated ([van Dishoeck & Black 1988](#)) ISRF, we use

$$G_{\text{eff}} = G_0 \times \exp(-2.5 A_V), \quad (5)$$

with the 3D-averaged  $A_{V,3D}$  provided by `TREERAY/OPTICALDEPTH`. This is an approximation of the direct line-of-sight visual extinction between a gas cell and the FUV emitting cluster, which we make due to computational memory considerations. The resulting effective local FUV field,  $G_{\text{eff}}$ , is variable in space and time.

To be consistent with the calculation of the local dust attenuation, we also limit the maximum distance a star cluster can contribute a non-zero FUV field to any surrounding cell to  $R = d = 50 \text{pc}$ . Hence,

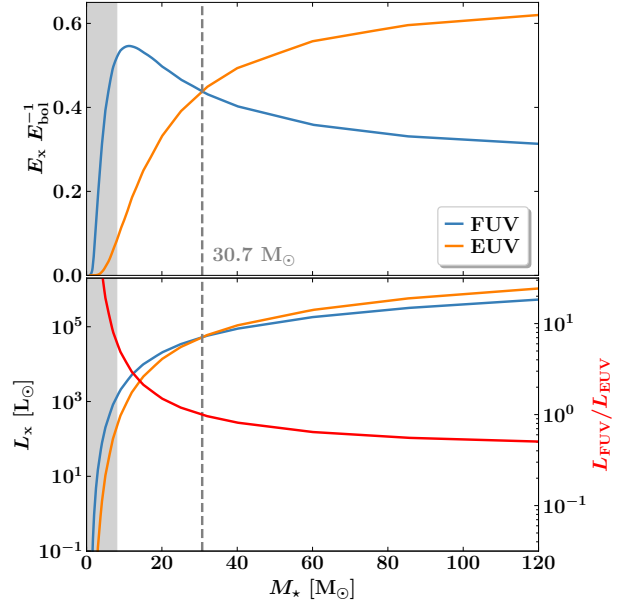


**Figure 1.** Assessment of the energetic importance of FUV radiation compared to EUV radiation from stars. *Top:* Total energy in the FUV plus EUV bands,  $E_x$ , normalised to the total bolometric energy of the respective star,  $E_{\text{bol}}$ , for different stars with stellar mass  $M_{\star}$ . *Bottom:* Total luminosity in the two respective energy bands as a function of stellar mass and the ratio of those luminosities (red line, right-hand y-axis). The FUV and EUV energy outputs are computed by assuming the stars as black bodies with effective temperatures taken from the Geneva stellar evolution tracks for stars that just entered the zero-age main sequence ([Ekström et al. 2012](#)). The grey-shaded area indicates the range of lower-mass stars ( $< 9 \text{M}_{\odot}$ ) which have not been individually tracked in our stellar evolution models. The vertical dashed line indicates the mass for which the EUV radiation band overtakes the FUV radiation band in terms of energy output. Even though FUV radiation cannot ionise atomic hydrogen, it is evident that the FUV radiation band is energetically important and cannot be neglected, especially for lower-mass stars.

only cells with cell centres within radius  $R = d$  of any given cluster are illuminated with the sum  $G_0$  (see Eq. 4). The distance  $d$  is a free model parameter and its implications are discussed in Appendix B.

In our chemical network,  $G_{\text{eff}}$  is included in several chemical reactions (e.g. to determine the  $\text{C}^+$  abundance) and, most importantly, in several heating rates such as PE heating. All relevant rates and reactions that depend on the strength of the FUV field can be found in Appendix C.

## 2.1 Far-ultraviolet luminosity of star clusters

This subsection describes how the FUV radiation field from star clusters with different masses is computed using `STARBURST99` ([Leitherer et al. 1999](#)). We show several tests that validate our treatment of the FUV radiation. Previously, we only explicitly tracked massive stars with  $M \geq 9 \text{M}_{\odot}$  in our star cluster sink particles. We follow the evolution of those stars ([Ekström et al. 2012](#)) and account for their individual stellar feedback ([Gatto et al. 2017](#); [Haid et al. 2018](#); [Rathjen et al. 2021](#)). Lower-mass stars have been aggregated within the star cluster sink particle and were only considered for their mass. Since they do not exhibit strong stellar winds, do not explode as supernovae, and only have a negligible contribution to the EUV radiation field, their impact has so far been negligible in our modelling.

In Fig. 1 (top panel), we show the fraction of FUV and EUV en-

ergy relative to the bolometric radiative energy as a function of the stellar mass  $M_\star$  of the source. In the bottom panel, we plot the corresponding FUV and EUV luminosities as a function of  $M_\star$ , and the right-hand y-axis shows the ratio of the two. The grey band indicates the regime of intermediate- and low-mass stars  $M_\star < 9 M_\odot$ . The dashed vertical line shows  $M_\star = 30.7 M_\odot$ , where we find that FUV and EUV radiation are energetically equally important. It is obvious that stars with masses below  $9 M_\odot$  cannot be neglected for the total FUV luminosity of a star cluster as it is usually done for EUV radiation. Therefore, we need to modify our star cluster subgrid model to account for low- and intermediate-mass stellar population.

Whenever we accrete  $120 M_\odot$  of gas onto a star cluster sink particle, we form one massive star with  $9 M_\odot \leq M_\star < 120 M_\odot$ , randomly sampled from an IMF with a Salpeter-IMF slope in the high-mass regime (Gatto et al. 2017). The left-over mass,  $M_{10} = (120 M_\odot - M_\star)$ , is assumed to form low- and intermediate-mass stars with  $< 9 M_\odot$  that we do not track individually. We use STARBURST99 to calculate the FUV luminosities of the low-mass stellar population of any given mass  $M_{10}$ . For the STARBURST99 model, we assume a total star cluster mass of  $10^6 M_\odot$  fully sampled with a Kroupa IMF (Kroupa 2001) starting with  $0.1 M_\odot$  and truncated at  $9 M_\odot$ . We use the Geneva tracks for solar metallicity and model the evolution to a maximum age of up to 200 Myr (which exceeds the maximum simulated time of  $t - t_{\text{SFR}} \approx 180$  Myr for our longest running simulation). We then integrate the resulting spectra calculated by STARBURST99 over photon energies between 5.6 eV and 13.6 eV to obtain the total FUV luminosity of that fully sampled  $10^6 M_\odot$  star cluster. We then scale the resulting luminosity with  $M_{10}$  to obtain the amount that any given population of low- and intermediate-mass stars with a given  $M_{10}$  would contribute.

In addition, we also have to account for the FUV luminosity of our explicitly tracked massive stars (prior, we only tracked their EUV contribution for photon energies larger than 13.6 eV). We obtain the FUV contribution of each massive star with mass  $M_\star$  by integrating a black body spectrum with an effective temperature of that star (taken from the Geneva tracks) over the FUV energy range and dividing by the fully integrated black body spectrum (see Fig. 1). We then multiply this ratio with the total bolometric luminosity of that star (taken from the Geneva tracks) which yields the star's FUV luminosity. Adding the two FUV components together, i.e. the total FUV luminosity of a massive star ( $M_\star$ ) with an accompanying low-to-intermediate-mass stellar population with mass  $M_{10}$ , we obtain the time-dependent total FUV luminosity per unit  $120 M_\odot$  of formed stars.

## 2.2 Theoretical considerations for the far-ultraviolet radiation field

We give predicted model outputs for the variable FUV radiation field and how it would heat the ISM. In Fig. 2, we show the unattenuated,  $G_0$ , (top panel) and dust-attenuated,  $G_{\text{eff}}$ , (bottom panel) strength of the FUV radiation field generated by a single massive star of mass  $M_\star$  as a function of distance  $R$  to that star. Throughout this section, we always assume a visual extinction of  $A_V = 1$  at a distance of  $R = d = 50$  pc for the dust-attenuated FUV field  $G_{\text{eff}}$ . This would translate to an uniform environmental density of  $n_{\text{H}} \approx 12 \text{ cm}^{-3}$ . We indicate with white contour lines the galactic background  $G_{\text{bg}} = 0.0948$ , the canonical solar neighbourhood value of  $G_0 = 1.7$ , and  $G_0 = 42.7$ , which is the highest value for the ISRF parameter in our static  $G_0$  models (see Table 1).

We extend this consideration in Fig. 3, where we do the same analysis as in Fig. 2 but this time for fully sampled star clusters with

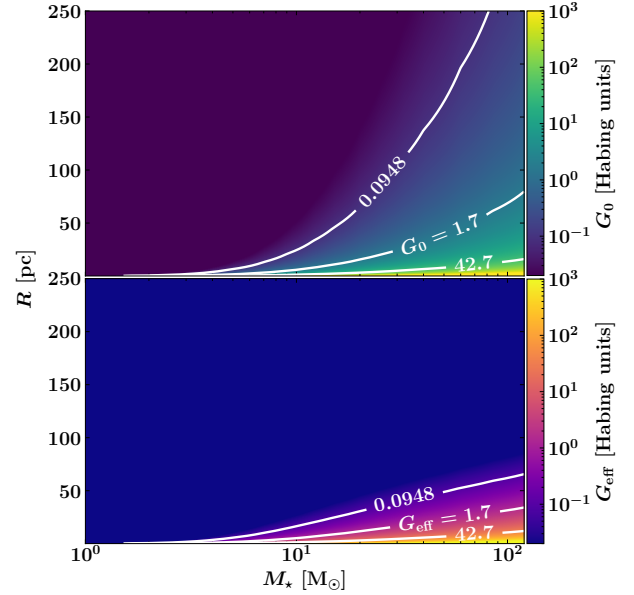


**Figure 2.** Strength of the FUV radiation field for the unattenuated ( $G_0$ , top panel) and attenuated ( $G_{\text{eff}}$ , bottom panel) cases as a function of distance  $R$  to a given single star and its respective mass,  $M_\star$ . For the attenuation, we assume a visual extinction of  $A_V = 1$  at a distance of 50 pc (i.e. the attenuation gets stronger further out and weaker closer in). This corresponds to a uniform hydrogen gas with a number density of  $n_{\text{H}} \approx 12 \text{ cm}^{-3}$ . The white contours indicate the assumed background FUV ISRF of  $G_{\text{bg}} = 0.0948$ , and, for comparison, the canonical solar neighbourhood value of  $G_0 = 1.7$  as well as the value of the constant ISRF previously used in simulations with high gas surface density ( $\Sigma_{100}$  with  $G_0 = 42.7$ , see Table 1). All values are in Habing units (see Sect. 2).

masses ranging between  $M_{\text{cluster}} = 200 - 10^6 M_\odot$ . The single stars, as well as the sampled clusters, are assumed to have just entered the main sequence ( $t_{\text{zams}} = 0$  Myr). Both, distance to the emitting source and attenuation by dust play a critical role in setting the strength of the FUV radiation field. For fairly massive star clusters with  $M_{\text{cluster}} \approx 10^4 M_\odot$ ,  $G_{\text{eff}}$  drops to roughly  $G_{\text{bg}}$  at a distance of 50 pc. Without attenuation by dust, the strength of the ISRF would not fall below  $G_{\text{bg}}$  at distances over  $R > 250$  pc (which is equal to half the box size of our computational domain with  $L_x = L_y = 500$  pc). We also indicate the maximum average star cluster masses in our simulations as vertical dashed lines, colour-coded by the initial conditions of the respective model (blue, orange, and pink dashed lines for runs with gas surface densities  $\Sigma_{\text{gas}} = 10, 30, \text{ and } 100 M_\odot \text{ pc}^{-2}$ , see Table 1 for details).

The stellar population within a star cluster is not static in time. Less massive stars live longer but have a lower luminosity output compared to the high-mass stars which have an expected lifetime between  $\tau_{\text{life}} \sim 3 - 30$  Myr (see e.g. Agertz et al. 2013, on how feedback evolves with cluster age). This shapes the radiation spectrum of the stellar cluster and has therefore also an impact on the overall energy density in the FUV band. In Fig. 4, we study after which time the FUV field strength of a stellar cluster with initial mass  $M_{\text{cluster}}$  at distance  $R$  drops below  $G_{\text{bg}}$ . The top panel shows the unattenuated case while the bottom panel shows the case accounting for extinction by dust. The region coloured in white indicates that for that configuration of  $M_{\text{cluster}}$  and  $R$  the FUV field strength would not drop below  $G_{\text{bg}}$  within 200 Myr of stellar evolution within the cluster. The long-lived lower-mass stars provide a significant amount of the total FUV energy density. Only very massive star clusters ( $M_{\text{cluster}} \gtrsim 3 \times 10^5 M_\odot$ ) would have a

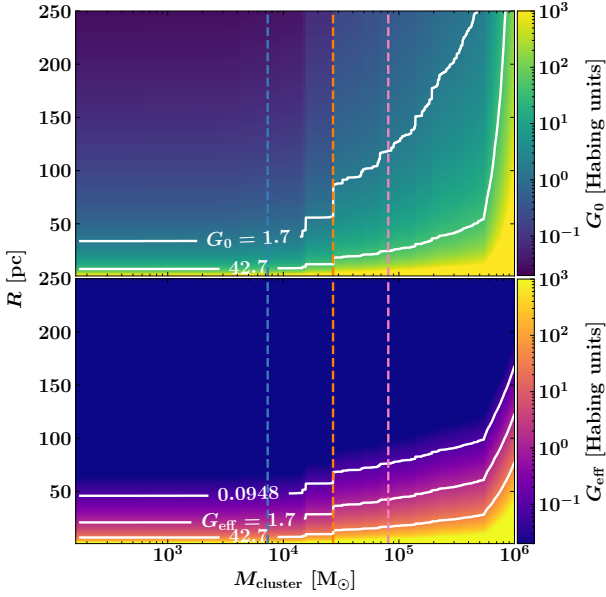


**Figure 3.** Same as in Fig. 2 but for star clusters with masses up to  $M_{\text{cluster}} = 10^6 M_{\odot}$ . We sample an IMF with a Salpeter-like slope for stars more massive than  $1 M_{\odot}$  to populate the star cluster. All stars are assumed to be on the zero-age main sequence. As a reference, we indicate the average mass of the formed star clusters in our simulations with varying initial conditions (see text and Table 1 for details). The unattenuated radiation field ( $G_0$ , top panel) never drops below our assumed background value  $G_{\text{bg}}$  for star clusters more massive than  $200 M_{\odot}$ . However, the dust attenuation (bottom panel) substantially reduces the local FUV field as a function of  $R$ .

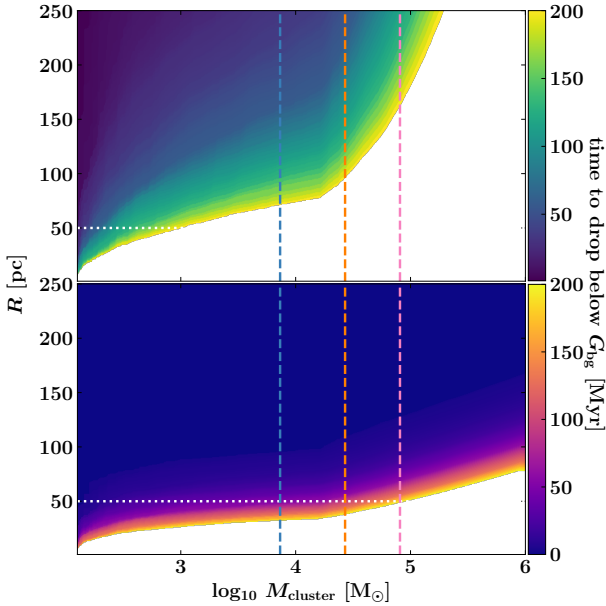


**Figure 4.** Time evolution of the strength of the FUV radiation field. We show the time after which the radiation field in the unattenuated case (top panel) and attenuated case (bottom panel) drop below  $G_{\text{bg}}$  as a function of cluster mass,  $M_{\text{cluster}}$ , and distance  $R$ . White areas mean that the radiation field strength never drops below  $G_{\text{bg}}$ . The vertical dashed lines show the maximum average mass of the formed star clusters in runs with different initial gas surface densities (see text and Table 1). The horizontal white dotted line indicates an FUV propagation distance of  $d = 50$  pc. We again assume an  $A_V = 1$  at  $d = 50$  pc, which translates to density of  $n_{\text{H}} \approx 12 \text{ cm}^{-3}$ .

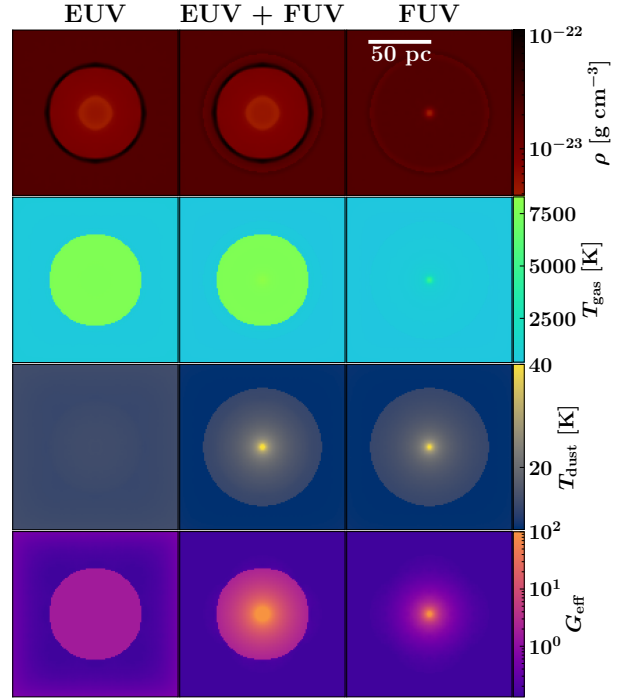


**Figure 5.** Isolated test of a single  $46 M_{\odot}$  star in a uniform and purely atomic hydrogen medium with  $n_{\text{H}} = 12 \text{ cm}^{-3}$  shown after 2 Myr of evolution. From top to bottom, we plot the total gas density,  $\rho$ , the kinetic gas temperature,  $T_{\text{gas}}$ , the dust temperature,  $T_{\text{dust}}$ , and  $G_{\text{eff}}$ . For this particular test, we compare models with only ionising radiation (EUV, first column), ionising plus FUV radiation (EUV + FUV, second column), and only self-consistent FUV radiation (FUV, third column). For the calculation of  $G_{\text{eff}}$  we use a value of  $G_0 = 1.7$  in the EUV-only case (first column).

non-negligible contribution to the FUV radiation field at distances  $R > 50$  pc when they enter the zero-age main sequence. Those super-massive star clusters are rare. The overall maximum cluster mass in our different models ranges between  $\max(M_{\text{cluster}}) \approx 3 \times 10^4 - 3 \times 10^5 M_{\odot}$ . The colour-coded vertical dashed lines in Fig. 3 and Fig. 4 indicate the average star cluster mass in our simulations with varying initial conditions (see Table 1 for details). Typical star clusters in our simulation, even at the most extreme conditions, emit a FUV radiation field which drops below  $G_{\text{bg}} = 0.0948$  at a distance of  $d = 50$  pc under the assumption of a moderate visual extinction of  $A_V = 1$  at that distance. This is especially true when also considering the time evolution of the star cluster. These figures demonstrate that limiting the maximum propagation range of the clusters' FUV radiation field to  $d = 50$  pc is a reasonable choice. This limit is compatible with dust attenuation calculations and would not significantly underpredict the far-away FUV ISRF. We discuss and test this assumption and model parameter further in Appendix B.

We study the impact of a self-consistent treatment of the FUV radiation field on the ISM with an idealised test of an isolated single  $46 M_{\odot}$  star in a uniform medium in Fig. 5. The simulation box encompasses  $(150 \text{ pc})^3$ . The gas is assumed to consist of purely atomic hydrogen with a hydrogen number density of  $n_{\text{H}} \approx 12 \text{ cm}^{-3}$  with an initial gas temperature of  $T_{\text{gas}} \approx 160$  K. The initial dust temperature is  $T_{\text{dust}} = 10$  K. This density is chosen so that the visual extinction at a distance of 50 pc is  $A_V(50 \text{ pc}) = 1$ . All stellar feedback is turned off, except for ionising radiation (EUV, first column), FUV plus EUV radiation (middle column), and only FUV radiation (right column). We let the system evolve for 2 Myr and show (from top

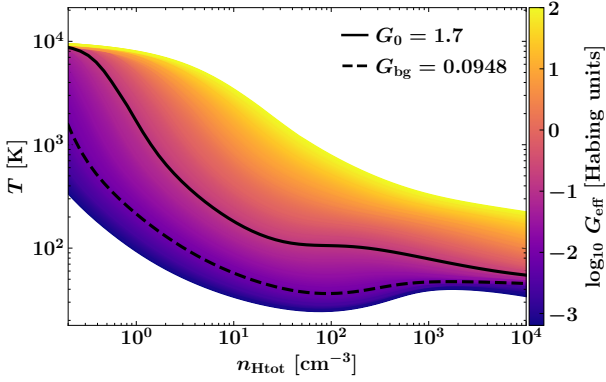


**Figure 6.** Equilibrium cooling curves computed with our chemical network. For all calculations, we assume a constant shielding by an external atomic hydrogen column density of  $N_{\text{H}} = 1.87 \times 10^{21} \text{ cm}^{-2}$  which translates to a visual extinction of  $A_{\text{V}} = 1$ . We show the cooling curves over a range of  $G_0 \approx 10^{-2} - 10^3$  ( $G_{\text{eff}} \approx 10^{-3} - 10^2$ ) in Habing units. Additionally, the gas is heated through the ionisation of hydrogen by CNMs with a CNM ionisation rate of  $\zeta_{\text{CR}} = 3 \times 10^{17} \text{ s}^{-1}$ . The solid black line shows the cooling curve for the canonical value  $G_0 = 1.7$  while the value corresponding to the model with  $G_0 = G_{\text{bg}} = 0.0948$  is depicted with a dashed black line. At higher number densities, necessary for star formation ( $n_{\text{H}} > 10^3 \text{ cm}^{-3}$ ), the equilibrium temperatures differ only by a factor of  $4.3 \pm 0.4$ , even though  $G_0$  varies over four orders of magnitude.

to bottom) slices of the gas density,  $\rho$ , the gas temperature,  $T_{\text{gas}}$ , the dust temperature  $T_{\text{dust}}$  and the strength of the FUV radiation field,  $G_{\text{eff}}$ . All quantities are presented as slices through the domain centre. We use a value of  $G_0 = 1.7$  when calculating  $G_{\text{eff}}$  in the EUV-only case. The FUV radiation field strongly impacts the dust temperature, which is very sensitive to the strength of  $G_{\text{eff}}$ . However, in the FUV-only case, the gas remains largely unaffected except for a moderate increase in temperature at the centre of the domain near the star particle. The PE heating is negligible compared to the effects of photoionisation, which heats the gas to the expected  $T \sim 8000 \text{ K}$ .

To understand the rather marginal impact of PE heating (as compared to heating by photoionisation), we explore equilibrium cooling curves derived for a range of  $G_0 = 10^{-2} - 10^3$  using our chemical network in Fig. 6. This calculation assumes constant shielding by an external atomic hydrogen column density of  $N_{\text{H}} = 1.87 \times 10^{21} \text{ cm}^{-2}$  ( $A_{\text{V}} = 1$ ) and additional heating by CRs using a  $\zeta_{\text{CR}} = 3 \times 10^{17} \text{ s}^{-1}$ . We highlight the cooling curve for  $G_0 = 1.7$  and  $G_0 = G_{\text{bg}} = 0.0948$  with a solid and dashed black line. Especially for higher densities, the equilibrium temperature is a weak function of  $G_0$  due to the exponential attenuation. At densities larger than our required threshold density for star formation,  $n_{\text{thr}} \approx 10^3 \text{ cm}^{-3}$ , a change in  $G_0$  over four orders of magnitude results in a change of the equilibrium temperature by just a factor of  $(4.3 \pm 0.4)$ . In strong FUV radiation fields ( $G_0 \sim 50 - 100$ ), within exposed (unshielded) environments and at moderately diffuse gas densities (total hydrogen nuclei number density  $n_{\text{H,tot}} \sim 1 \text{ cm}^{-3}$ ), PE heating can raise gas temperatures to levels comparable to those produced by photoionisation ( $T \sim 10^4 \text{ K}$ ).

We further investigate the PE heating rate,  $\Gamma_{\text{PE}}$ , normalised to the  $\Gamma_{\text{PE}}$  at constant  $G_0 = 1.7$ ,  $\Gamma_{\text{PE}, 1.7}$ , as a function of  $G_{\text{eff}}$ . For  $\Gamma_{\text{PE}}$ , we follow the prescription of Bakes & Tielens (1994) and Bergin et al. (2004):

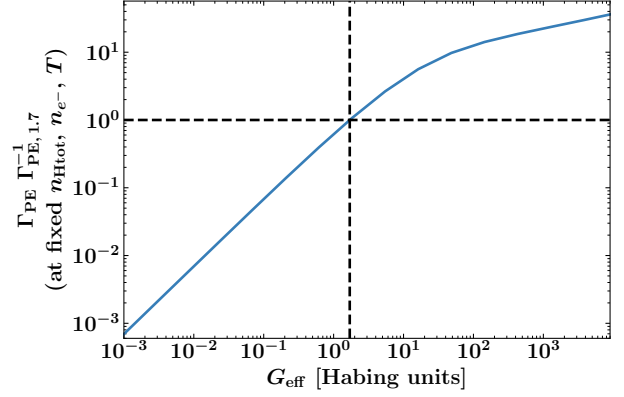


**Figure 7.** PE heating rate,  $\Gamma_{\text{PE}}$ , as a function of  $G_{\text{eff}}$ , normalised to  $\Gamma_{\text{PE}, 1.7}$  for  $G_{\text{eff}} = 1.7$  at fixed hydrogen number density,  $n_{\text{H,tot}}$ , electron number density,  $n_{\text{e}^-}$ , and temperature,  $T$ . We indicate the values for  $G_{\text{eff}} = 1.7$  for reference with dashed lines. The PE heating rate first scales linearly with  $G_{\text{eff}}$ , but then increases more slowly for  $G_{\text{eff}} \gtrsim 10$ .

$$\Gamma_{\text{PE}} = 1.3 \times 10^{-24} \cdot \epsilon \cdot G_{\text{eff}} \cdot n_{\text{H,tot}} \quad (6)$$

$$\epsilon = 0.049 \cdot \left(1 + (\Psi/963)^{0.73}\right)^{-1} + \left(0.037 \cdot (T/10^4)^{0.7}\right) \cdot \left(1 + 4 \times 10^{-4} \cdot \Psi\right) \quad (7)$$

$$\Psi = G_{\text{eff}} \cdot \sqrt{T} \cdot n_{\text{e}^-}^{-1}, \quad (8)$$

with the PE heating efficiency,  $\epsilon$  (Wolfire et al. 2003), electron number density,  $n_{\text{e}^-}$ , and total hydrogen number density,  $n_{\text{H,tot}}$ . In Fig. 7, we show the normalised  $\Gamma_{\text{PE}} \Gamma_{\text{PE}, 1.7}^{-1}$  as a function of  $G_{\text{eff}}$  at fixed hydrogen and electron number densities and gas temperature. Dashed lines indicate the normalised  $\Gamma_{\text{PE}}$  where  $G_{\text{eff}} = 1.7$ . For low FUV radiation field strengths,  $\Gamma_{\text{PE}}$  scales linearly with  $G_{\text{eff}}$ . For  $G_{\text{eff}} \gtrsim 10$ , this behaviour changes significantly and  $\Gamma_{\text{PE}}$  flattens out. This explains the marginal heating capabilities of the FUV radiation field beyond temperatures of  $\sim 10^3 \text{ K}$ .

### 2.3 Initial conditions and parameters of the simulations

We discuss a series of nine high-resolution MHD simulations of the multiphase ISM in a stratified galactic patch. The simulations are part of the SILCC PROJECT simulation framework and closely follow the setup of Rathjen et al. (2023). The key addition to Rathjen et al. (2023) is the new module ADAPTIVEG0 to evaluate the ISRF FUV radiation field produced by star clusters. The set of simulations is designed to explore the complex and non-linear effects of incorporating a self-consistent FUV radiation field generated by stellar clusters – the novel ADAPTIVEG0 module – on the SFR and ISM chemistry.

The computational domain of the simulated galactic patch spans  $(500 \times 500 \times \pm 4000) \text{ pc}^3$  with a base AMR grid resolution of  $dx \approx 3.9 \text{ pc}$  in the midplane. We implement periodic boundary conditions along the  $x$ - and  $y$ -directions and outflow boundaries along the elongated  $z$ -direction. With this setup, we aim to mimic a patch cut out of a galactic disc. Initially, the gas is in hydrostatic equilibrium and is set up with a Gaussian density distribution around the midplane. Together with the initial gas surface density,  $\Sigma_{\text{gas}}$ , we vary the thickness of the Gaussian gas disc,  $\sigma_{\text{gas}}$ , the initial magnetic field strength,  $|\mathbf{B}|$ , the strength of the initial turbulent driving,  $v_{\text{rms}}$ , and the CRIR,  $\zeta_{\text{CR}}$ , to model different galactic environments. The initial

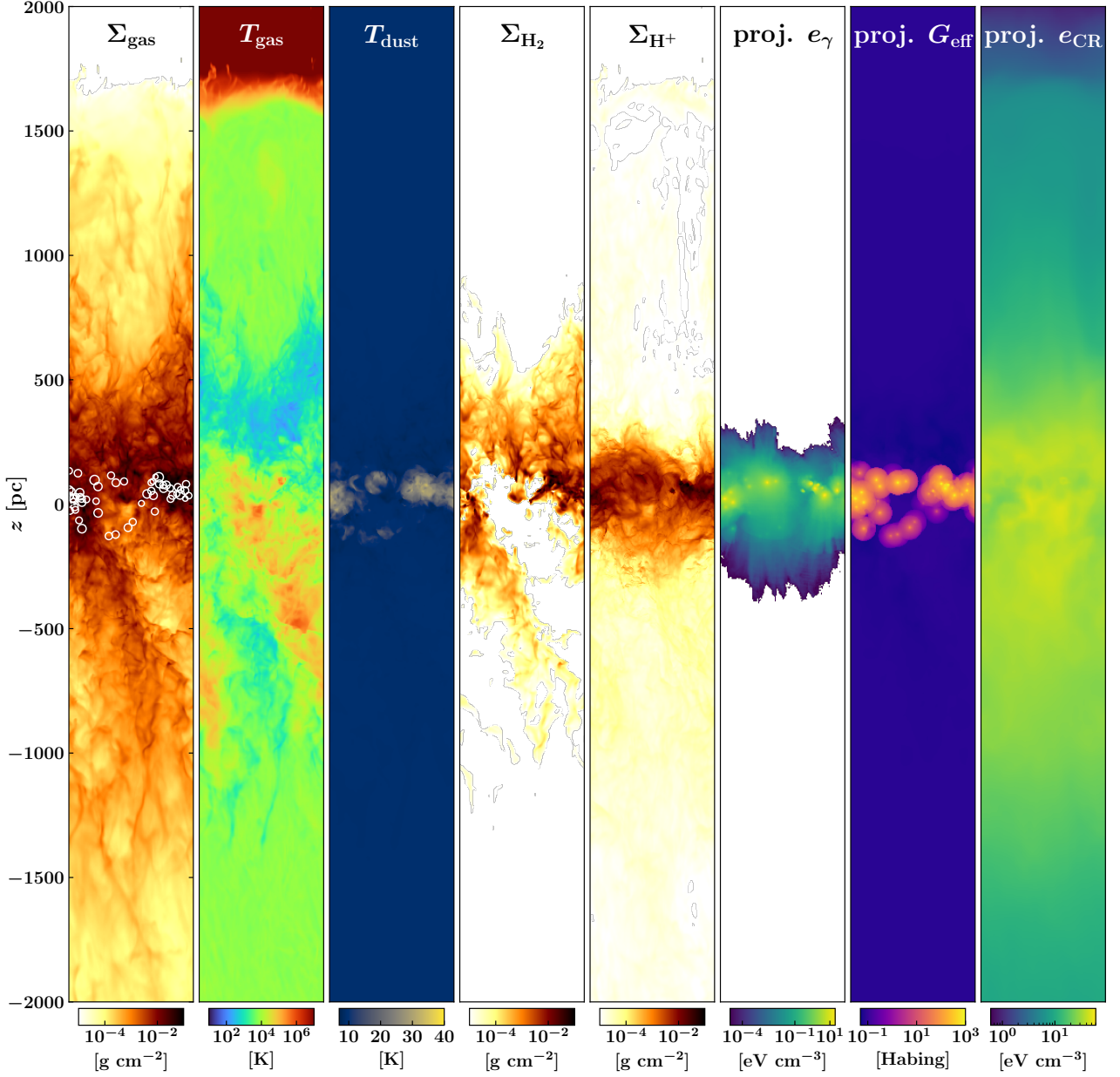


**Figure 8.** Overview of  $\Sigma_{100vFUV}$  at  $t - t_{\text{SFR}} = 30$  Myr. Shown are the edge-on views of the total gas ( $\Sigma_{\text{gas}}$ , 1<sup>st</sup> panel), molecular hydrogen ( $\Sigma_{\text{H}_2}$ , 4<sup>th</sup> panel) and ionised hydrogen ( $\Sigma_{\text{H}^+}$ , 5<sup>th</sup> panel) surface densities, as well as mass-weighted gas ( $T_{\text{gas}}$ , 2<sup>nd</sup> panel) and dust ( $T_{\text{dust}}$ , 3<sup>rd</sup> panel) temperatures, ionising photon energy density ( $e_\gamma$ , 6<sup>th</sup> panel), the effective  $G_0$  field ( $G_{\text{eff}}$ , 7<sup>th</sup> panel), and CNM energy density ( $e_{\text{CR}}$ , 8<sup>th</sup> panel) in projection. The star-forming galactic ISM is concentrated around the midplane. White circles in the 1<sup>st</sup> panel indicate active star clusters.

turbulent driving in each simulation prevents the gas disc from collapsing into a single dense sheet and triggers star formation. Once star formation begins and the ISM self-regulates via stellar feedback, the artificial turbulent driving is turned off.

We present three simulations with  $\Sigma_{\text{gas}} = 10, 30, \text{ and } 100 M_\odot \text{pc}^{-2}$  to model different galactic environments, and which include the `ADAPTIVEG0` module. These are compared to a set of three simulations with the same initial conditions but using the static ISRF<sup>1</sup>.

<sup>1</sup> We note that we account for extinction by dust in both cases. In the case of a static ISRF, the specified strength, e.g.  $G_0 = 1.7$  for model  $\Sigma_{10}$ ,

Both sets of simulations include all major stellar feedback channels, stellar winds, EUV radiation, and SNe. CR acceleration in SN remnants with 10 per cent efficiency ( $E_{\text{CR}} = 0.1 E_{\text{SN}} = 10^{50}$  erg) and their anisotropic diffusion along the magnetic field is considered in all models.

Lastly, we present three more simulations, two with `ADAPTIVEG0`

represents the baseline FUV ISRF, which remains constant in space and time but undergoes dust attenuation in each computational cell. Locally, the ISRF cannot exceed this baseline value, though it may be significantly reduced in regions with high optical depth. For higher initial  $\Sigma_{\text{gas}}$ , the baseline value is also increased.

**Table 1.** List of simulations with their varying initial parameters. From left to right, we give the name of each simulation, the initial gas surface density,  $\Sigma_{\text{gas}}$ , whether we use the novel ADAPTIVEG0 module or a constant FUV ISRF with  $G_0$ , the initial strength of the magnetic field,  $|\mathbf{B}|$ , the thickness of the initial Gaussian gas density profile,  $\sigma_{\text{gas}}$ , the target root mean square velocity of the initial turbulent driving,  $v_{\text{rms}}$ , and the value of the constant CR ionisation rate,  $\zeta_{\text{CR}}$ . Except for the last three models, all simulations utilise all stellar feedback processes (winds, ionising radiation, SNe), and CRs. Models without ionising radiation nor stellar winds are labelled with the †-suffix ( $\Sigma 010\text{vFUV}\dagger$  and  $\Sigma 010\dagger$ ). The model  $\Sigma 010\text{vFUV}\dagger$  includes SNe, CRs, and ADAPTIVEG0. The model  $\Sigma 010\dagger$  includes only SNe and CRs. Finally, the model  $\Sigma 010\text{vFUVnoSN}\dagger$  only includes ADAPTIVEG0 without any other feedback processes.

Name	$\Sigma_{\text{gas}}$ [ $M_{\odot} \text{ pc}^{-2}$ ]	$G_0$ [Habing]	$ \mathbf{B} $ [ $\mu\text{G}$ ]	$\sigma_{\text{gas}}$ [pc]	$v_{\text{rms}}$ [ $\text{kms}^{-1}$ ]	$\zeta_{\text{CR}}$ [ $\text{s}^{-1}$ ]
$\Sigma 010\text{vFUV}$	10	ADAPTIVEG0	6	30	10	$3 \times 10^{-17}$
$\Sigma 030\text{vFUV}$	30	ADAPTIVEG0	10	37	15	$9 \times 10^{-17}$
$\Sigma 100\text{vFUV}$	100	ADAPTIVEG0	19	60	30	$3 \times 10^{-16}$
$\Sigma 010$	10	1.7	6	30	10	$3 \times 10^{-17}$
$\Sigma 030$	30	7.9	10	37	15	$9 \times 10^{-17}$
$\Sigma 100$	100	42.7	19	60	30	$3 \times 10^{-16}$
$\Sigma 010\text{vFUV}\dagger$	10	ADAPTIVEG0	6	30	10	$3 \times 10^{-17}$
$\Sigma 010\dagger$	10	1.7	6	30	10	$3 \times 10^{-17}$
$\Sigma 010\text{vFUVnoSN}\dagger$	10	ADAPTIVEG0	6	30	10	$3 \times 10^{-17}$

and one with a static ISRF. In these models, we turn off the stellar wind and EUV radiation feedback. In Rathjen et al. (2021) and Rathjen et al. (2023), we show that these early stellar feedback mechanisms are likely the primary self-regulation processes for star formation. By omitting them, we can further investigate how capable FUV radiation from young massive star clusters is in reducing further gas accretion onto the cluster and therefore reducing the SFR. In two of the three models,  $\Sigma 010\text{vFUV}\dagger$  and  $\Sigma 010\dagger$ , SN feedback is still turned on. In the model  $\Sigma 010\text{vFUVnoSN}\dagger$ , we also switch off SN feedback and only consider the FUV radiation feedback channel. All simulations<sup>2</sup> and their varying initial parameters are summarised in Table 1.

We give a general overview of our setup in Fig. 8. We define the onset of star formation,  $t_{\text{SFR}}$ , as the moment when the ISM starts to regulate itself and show the run  $\Sigma 100\text{vFUV}$ , 30 Myr after the onset of star formation, at  $t - t_{\text{SFR}} = 30$  Myr. Due to formatting reasons, we chose only to show the simulation domain for  $|z| \leq 2$  kpc (instead of the full box,  $z = \pm 4$  kpc). Horizontally, we show the full extent ( $x = 500$  pc). We present, from left to right: the total gas column density,  $\Sigma_{\text{gas}}$ , the projected mass-weighted gas temperature,  $T_{\text{gas}}$ , and projected mass-weighted dust temperature,  $T_{\text{dust}}$ , the molecular hydrogen column density,  $\Sigma_{\text{H}_2}$ , the ionised hydrogen column density,  $\Sigma_{\text{H}^+}$ , a volume-weighted projection of the ionising radiation energy density,  $e_{\gamma}$ , a volume-weighted projection of the ISRF strength,  $G_{\text{eff}}$ , and finally a volume-weighted projection of the CR energy density,  $e_{\text{CR}}$ . Star cluster sink particles are represented as white circles in the first panel. The depicted size scales with the star clusters' mass and does not represent the star clusters' physical extent. The ISM

<sup>2</sup> We note that the models  $\Sigma 010$ ,  $\Sigma 030$ ,  $\Sigma 100$  have previously been published in Rathjen et al. (2023) under the same name. We include them here for comparison.

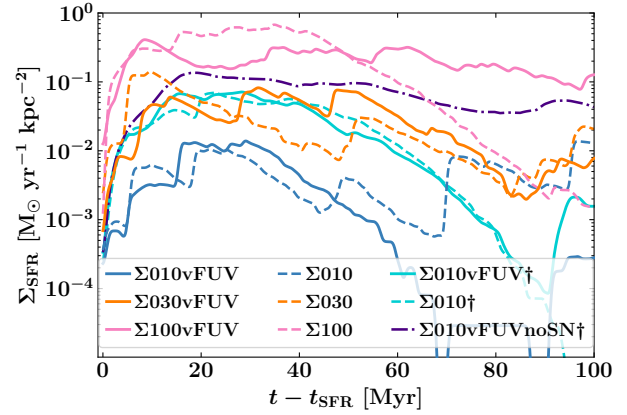


**Figure 9.** Star formation rate surface density,  $\Sigma_{\text{SFR}}$ , as a function of simulated time after the onset of star formation,  $t - t_{\text{SFR}}$ . Runs with the ADAPTIVEG0 model are shown in solid lines while their static  $G_0$  counterparts are depicted with dashed lines. We also include two simulations with only SN feedback (cyan dashed) and SN+FUV feedback (cyan solid). In SN-only runs, an adaptive  $G_0$  makes virtually no difference to the SFR (see similarity of the two cyan lines). The purple dash-dotted line shows a model at solar neighbourhood conditions without any feedback but the variable FUV radiation via ADAPTIVEG0. Self-consistent FUV feedback does not seem to efficiently regulate star formation and produce  $\Sigma_{\text{SFR}}$  in line with predictions motivated by observations.

is multiphase with molecular hydrogen (4<sup>th</sup> panel) forming in cold regions ( $T < 300$  K, blueish regions in the 2<sup>nd</sup> panel). Most of the volume is filled by the WNM ( $300 < T \leq 3 \times 10^5$  K,  $\chi_{\text{ion}} < 0.5$ ) and the warm ionised medium (WIM,  $300 < T \leq 3 \times 10^5$  K,  $\chi_{\text{ion}} \geq 0.5$ ) at temperatures around  $T \approx 10^4$  K. Overlapping SN remnants generate pockets of hot gas with temperatures exceeding  $T \gtrsim 3 \times 10^5$  K. Strong CR-supported outflows, which can lift the gas to heights up to 2 kpc, are present.

## 3 RESULTS

### 3.1 Star formation

In Fig. 9, we show the time evolution of the star formation rate surface density,  $\Sigma_{\text{SFR}}$ . The data is presented up to  $t - t_{\text{SFR}} = 100$  Myr. Note that  $t_{\text{SFR}}$  is different for each model (between  $\sim 5 - 20$  Myr). Solid lines indicate models that include the ADAPTIVEG0 module, while dashed lines represent the respective models with static  $G_0$ . The two models shown with cyan colour are the runs without early stellar feedback in the form of stellar winds and ionising radiation. We do not observe any distinct trends that would indicate the impact of the locally varying FUV radiation on  $\Sigma_{\text{SFR}}$  across different galactic environments. Models with and without ADAPTIVEG0 closely follow each other. For each pair of models with equal  $\Sigma_{\text{gas}}$ , there are periods in time where  $\Sigma_{\text{SFR}}$  of one model is higher/lower than the other, but those differences are most likely due to the highly non-linear stochastic nature of the star formation process. We want to especially highlight the nearly identical behaviour of the models  $\Sigma 010\text{vFUV}\dagger$  and  $\Sigma 010\dagger$  with respect to  $\Sigma_{\text{SFR}}$ . Massive star formation in those models is purely regulated by SNe and their  $\Sigma_{\text{SFR}}$  is about one order of magnitude higher than their counterparts including stellar winds and ionising radiation ( $\Sigma 010$  and  $\Sigma 010\text{vFUV}$ ). This is a clear indication of the importance of HII regions and massive-star winds in the process of regulating star formation. At the same time, the impact of the variable FUV field seems to be minimal. The model without any



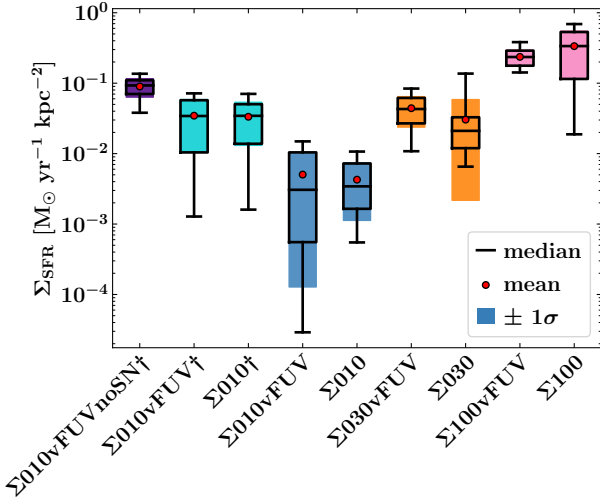


**Figure 10.** Star formation rate surface densities summarised as box plots. We calculate the values for a time evolution starting 10 Myr after the onset of star formation to minimise the possible impact of the numerical initial conditions on the first star formation episode. Red dots indicate the averaged  $\Sigma_{\text{SFR}}$  values. A standard deviation of  $\pm 1\sigma$  is shown as coloured shaded areas. The boxes span from the 25<sup>th</sup> to the 75<sup>th</sup> percentile and the whiskers indicate the minimum and maximum value of the time evolution. No clear trends for the impact of the variable FUV radiation are visible between the different simulation models.

stellar feedback besides variable FUV radiation,  $\Sigma010\text{vFUVnoSN}\dagger$ , stabilises at  $\Sigma_{\text{SFR}} \approx 10^{-1} \text{ M}_{\odot} \text{ yr}^{-1} \text{ kpc}^{-2}$ , which is approximately twice as high as that of the  $\Sigma010\text{vFUV}\dagger$  and  $\Sigma010\dagger$  models.

To better quantify the results of Fig. 9, we show the distribution of  $\Sigma_{\text{SFR}}$  for each model in Fig. 10 over a time frame of  $t - t_{\text{SFR}} = 10\text{--}100$  Myr. We start only 10 Myr after the onset of star formation to reduce the possible impact of the initial conditions. Each box plot in Fig. 10 encompasses the  $\Sigma_{\text{SFR}}$  data within the 25<sup>th</sup>- and 75<sup>th</sup>-percentiles. Thick black lines inside each box plot indicate the median value, whereas the time-averaged mean is shown as red dots. Coloured shaded areas show the standard deviation of the mean ( $\pm 1\sigma$ ). The whiskers show the minimum and maximum values of the time evolution. The integrated values of  $\Sigma_{\text{SFR}}$  do not differ with statistical significance. Between  $\Sigma010\text{vFUV}$  and  $\Sigma010\text{vFUV}\dagger$ ,  $\Sigma_{\text{SFR}}$  differs by one order of magnitude. Therefore, these results suggest that  $\Sigma_{\text{SFR}}$  is regulated by ionising radiation and hot wind bubbles, rather than by non-ionising radiation. Observations of local galactic star-forming regions obtained by Leroy et al. (2008) estimate  $\Sigma_{\text{SFR}} \approx 7.89 \times 10^{-3} \text{ M}_{\odot} \text{ yr}^{-1} \text{ kpc}^{-2}$  for  $\Sigma_{\text{gas}} \approx 10 \text{ M}_{\odot} \text{ pc}^{-2}$ . These observations, however, have a large scatter, especially at conditions similar to the solar neighbourhood. Models without stellar wind and ionising radiation feedback (purple and cyan) overestimate  $\Sigma_{\text{SFR}}$  relative to observational predictions.

The variable FUV radiation field causes a highly non-uniform PE heating rate within the computational domain. However, the impact of the FUV radiation feedback is clearly subdominant to photoionisation with respect to supporting the gas against further collapse, thus regulating the accretion of gas onto the cluster and, as a consequence, the SFR. The distribution of  $\Sigma_{\text{SFR}}$  over time in models without photoionisation and stellar winds ( $\Sigma010\text{vFUV}\dagger$  and  $\Sigma010\dagger$ ) is nearly identical. There are no consistent trends observed when comparing the models with the ADAPTIVEG0 module to those without it across different galactic environments. The ADAPTIVEG0 models can have

either higher or lower  $\Sigma_{\text{SFR}}$  compared to the static  $G_0$  models. This variable relationship holds true for all  $\Sigma_{\text{gas}}$  realisations.

At lower gas surface densities ( $\Sigma010$  and  $\Sigma010\text{vFUV}$ ), the addition of a self-consistent treatment of the FUV radiation field increases the spread in the  $\Sigma_{\text{SFR}}$  distribution, while at higher surface densities, the spread is reduced. The increased spread, measured as the interquartile range and standard deviation of the mean, between the solar neighbourhood models is most likely not due to the effects of potentially FUV-regulated local star formation but due to the sharp decrease of  $\Sigma_{\text{SFR}}$  in  $\Sigma010\text{vFUV}$  starting at  $t - t_{\text{SFR}} \sim 50$  Myr. We confirm this hypothesis in Appendix D, showing how this run evolves over a longer time. The standard deviation of  $\Sigma_{\text{SFR}}$ ,  $\sigma_{\text{SFR}}$ , can be interpreted as a tracer of the burstiness of star formation. The average  $\sigma_{\text{SFR}}$  in ADAPTIVEG0 models is reduced to  $87 \pm 44$  per cent of the averaged  $\sigma_{\text{SFR}}$  in the static  $G_0$  counterparts. If we exclude the  $\Sigma010$  models for reasons discussed in Appendix D, the reduction is even more pronounced, with  $62 \pm 32$  per cent.

We give a summary of the  $\Sigma_{\text{SFR}}$  data in Table A1 in Appendix A.

### 3.2 Gas structure

We investigate the effects of a time- and space-varying ISRF on the gas phase dynamics of the ISM. In Fig. 11, we display mass-weighted joint probability density functions (PDFs) of the gas temperature,  $T_{\text{gas}}$ , and the total number density of hydrogen nuclei,  $n_{\text{Htot}}$ . The left column shows models with ADAPTIVEG0, while the right column shows corresponding models with a static  $G_0$ . As a reference, equilibrium cooling curves are displayed for as solid black lines for  $G_0 = [1.7, 7.9, 42.7]$ , corresponding to  $G_{\text{eff}} = [0.14, 0.65, 3.51]$  (compare with Fig. 6) and for  $G_0 = G_{\text{bg}} = 0.0948$ . The gas phase distribution in models with a static  $G_0$  closely matches the equilibrium configuration, except for the HII region branch at  $T \sim 10^4$  K. Hot, low-density gas (upper left part of the phase diagrams) is shock-heated by SNe. The marginal amount of cold, low-density gas results from CRs, accelerated in SN remnants, and their diffusion. Additional CR pressure near embedded star clusters leads to gas expansion via adiabatic processes. However, after multiple SNe explode in an area, overlapping remnants thermalise the gas, rapidly heating it to temperatures above  $T \gtrsim 3 \times 10^5$  K. This scenario changes with a variable FUV radiation field. In static  $G_0$  models, most of the gas mass ( $67.1 \pm 3.2$  per cent) resides above their respective solid black  $G_0$  equilibrium cooling curve in the  $n_{\text{Htot}}\text{--}T_{\text{gas}}$  plane<sup>3</sup>. The majority of this gas is photoionised within HII regions. For ADAPTIVEG0 models, this is significantly different, with a total gas mass fraction (MF) of  $31.2 \pm 3.9$  per cent above the corresponding equilibrium phase. Due to the broad spatial variations of the FUV ISRF, the gas phase distribution broadens and smears out between indicated equilibrium states (solid line and dashed line). A distinct branch of cold ( $T < 300$  K) and diffuse ( $n_{\text{Htot}} \lesssim 1 \text{ cm}^{-3}$ ) gas containing a significant MF emerges. As in the static  $G_0$  case, CR pressure partially contributes to this. However, this diffuse, cold (and potentially molecular) gas mostly resides far from young massive star clusters, where it is not exposed to strong FUV radiation and now it is no longer heated by a static radiation field with  $G_0$ .

We further analyse this cold diffuse gas branch by examining another density-temperature phase diagram in Fig. 12, focusing this

<sup>3</sup> We want to note that these cooling curves are all a function of the external visual extinction,  $A_V$ . The curves depicted in Fig. 11 have been calculated for  $A_V = 1$ . Gas in more shielded regions would end up at a lower equilibrium temperature while more diffuse gas would be able to be heated more.

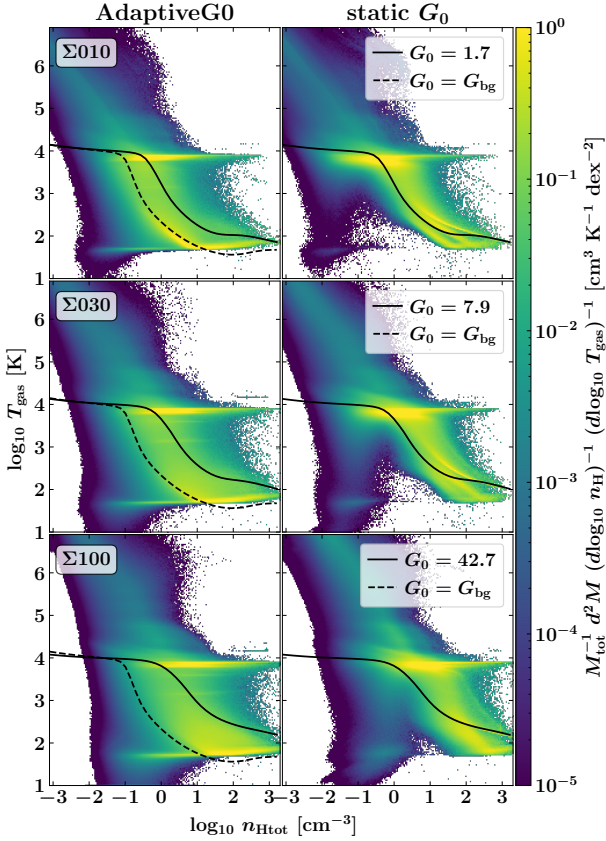


**Figure 11.** Joint probability density functions showing the gas mass distribution in the plane of the gas temperature,  $T_{\text{gas}}$  and the total hydrogen nuclei number density,  $n_{\text{Htot}}$ . We only show data near the disc midplane (defined as  $|z| \leq 500$  pc). We cover the time range from  $t - t_{\text{SFR}} = 10$  Myr till the end of the simulated time at  $t - t_{\text{SFR}} = 100$  Myr, to exclude initial condition effects. We show the static  $G_0$  models in the right column and indicate the equilibrium cooling curve for the given static  $G_0$  value as a solid black line. For the models with the ADAPTIVEG0 module (left column), we also indicate the equilibrium cooling curve for the corresponding static  $G_0$  (solid line), as well as the equilibrium cooling curve for the background  $G_{\text{bg}} = 0.0948$  (dashed line). For both cooling curves we assume an external shielding with  $A_V = 1$ , similar to Fig. 6. The wider range of potential cooling curves (also see Fig. 6) leads to a smeared-out temperature-density PDF for temperatures between a couple tens to  $10^4$  K.

time on molecular hydrogen gas density ( $n_{\text{H}_2}$ ). As a reference, the threshold molecular hydrogen density above which 90 per cent of all molecular hydrogen resides are indicated with vertical dashed lines in Fig. 12. In both scenarios, with and without ADAPTIVEG0, most molecular hydrogen gas is in a cold, dense phase<sup>4</sup>. Similar to Fig. 11, a self-consistent FUV radiation field broadens the temperature-density distribution in the ISM. Based on the 90 per cent  $\text{H}_2$  density threshold in the static  $G_0$  models (dashed blue vertical line in Fig. 12), we define diffuse  $\text{H}_2$  as  $n_{\text{H}_2} < 2 \text{ cm}^{-3}$  and dense/compact  $\text{H}_2$  as  $n_{\text{H}_2} \geq 2 \text{ cm}^{-3}$ . With this definition, the average MF of diffuse

<sup>4</sup> We note that we do not explicitly follow the gas phases of individual chemical species with tracer particles. For each cell in the computational domain, we know the total gas density, temperature, and MF of each chemical species included in the network (see Sect. 2). Gas mixing on scales smaller than  $\sim (4 \text{ pc})^3$  (corresponding to the resolution of the AMR grid in the midplane ISM) is not resolved.

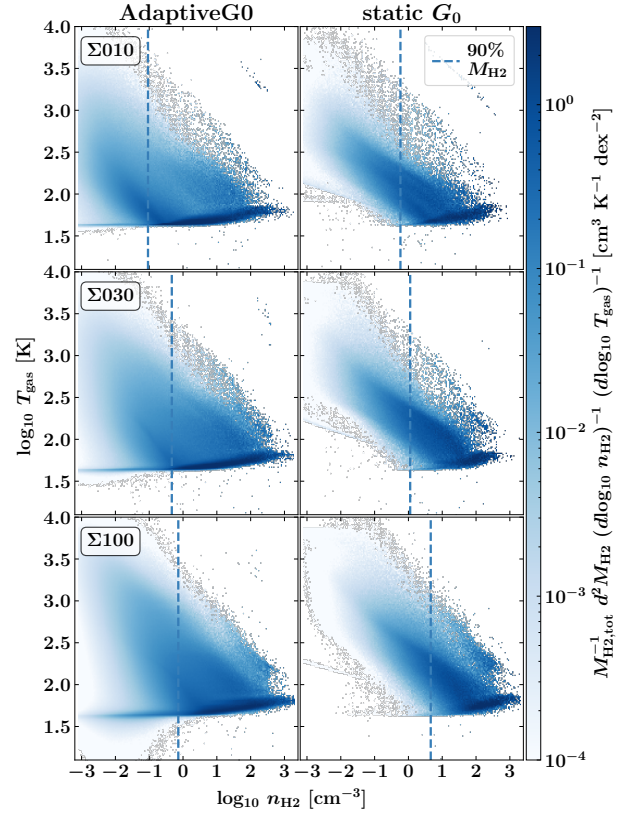


**Figure 12.** Same as Fig. 11 but for  $T_{\text{gas}}$  and molecular hydrogen number density,  $n_{\text{H}_2}$ . We indicate the  $\text{H}_2$  number density above which 90 per cent for the total molecular hydrogen gas mass,  $M_{\text{H}_2}$ , resides with vertical dashed lines. This threshold density is approximately one order of magnitude lower in the ADAPTIVEG0 cases compared to the static  $G_0$  counterparts. The variable FUV radiation field promotes the formation of a diffuse molecular hydrogen phase with temperatures below 100 K.

$\text{H}_2$  gas weighted by the total  $\text{H}_2$  mass in the ADAPTIVEG0 models is  $22.5 \pm 7.1$  per cent and  $8.9 \pm 6.2$  per cent in the static  $G_0$  models. We identify a clear anti-correlation of the diffuse  $\text{H}_2$  MF with  $\Sigma_{\text{gas}}$ , as it ranges from  $40.1 \pm 12.2$  per cent in  $\Sigma 010 \text{vFUV}$  down to  $20.4 \pm 2.7$  per cent in  $\Sigma 100 \text{vFUV}$ . A similar anti-correlation exists for the static  $G_0$  models. The diffuse, cold (and molecular) gas is present in the ADAPTIVEG0 models but is mostly absent in the static  $G_0$  runs. Nonetheless, most of the  $\text{H}_2$  gas still exists in high-density environments, especially at higher  $\Sigma_{\text{gas}}$ .

We focus on the dust density and temperature distribution in Fig. 13, similar to Fig. 11. We can show  $T_{\text{dust}}$  as a function of  $n_{\text{Htot}}$  because we adopt a constant dust-to-gas MF of 1 per cent in our chemical network. For a static radiation field, the dust temperature has a sharp upper limit between  $T_{\text{dust}} \approx 15 - 25$  K, depending on the strength of the static  $G_0$  field, which scales with the initial  $\Sigma_{\text{gas}}$  of each model. The temperature distributions are almost flat, with a slight trend to colder temperatures at higher densities because of an increasing extinction. With ADAPTIVEG0, the majority of the dust in the computational domain (by mass) has a temperature of  $T_{\text{dust}} \approx 10$  K, which reflects the temperature reached through heating with the background FUV radiation field  $G_{\text{bg}} = 0.0948$ . However, a significant amount of dust is heated to temperatures around  $T_{\text{dust}} \approx 60$  K. There is no clear correlation between the gas density (and therefore also dust density) and dust temperature. Still, most of the dust (by mass) resides in gas reservoirs with densities above  $n_{\text{Htot}} \gtrsim$

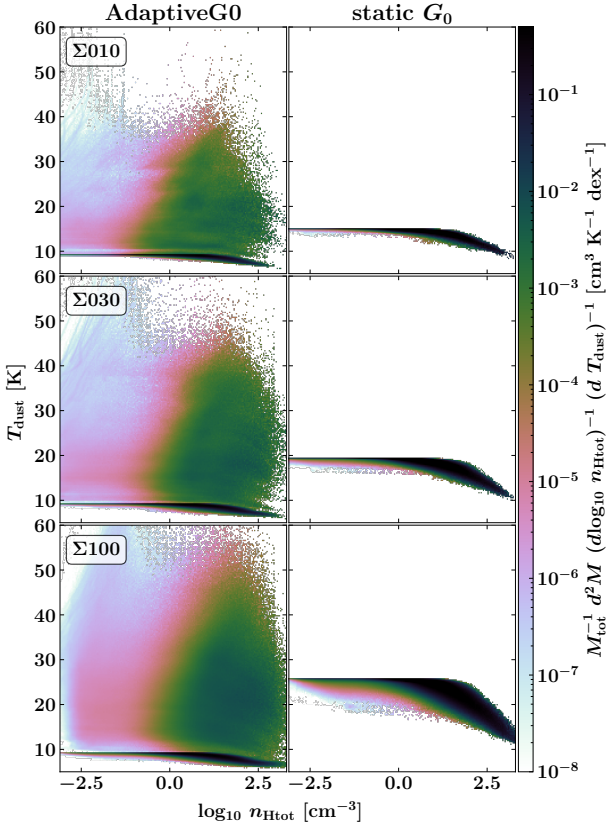


**Figure 13.** Joint probability density functions showing the mass distribution in the dust temperature,  $T_{\text{dust}}$ , and  $n_{\text{Htot}}$  plane. Since we employ a constant gas-to-dust mass ratio of one per cent,  $n_{\text{Htot}}$  is a tracer for  $n_{\text{dust}}$ . A large portion of the dust in all ADAPTIVEG0 models sits at lower temperatures compared to the static models due to lesser heating in regimes of  $G_{\text{eff}} = G_{\text{bg}}$ . However, dust closer to star-forming regions does not show a flat distribution as in the static models and can be heated up to 60 K via the PE effect. A wider spread in dust temperature can substantially impact synthetic observables deduced from our models.

$1 \text{ cm}^{-3}$ . The variations in  $T_{\text{dust}}$  are negligible for the gas dynamics in our models. Nonetheless, observables are strongly dependent on  $T_{\text{dust}}$  (see e.g. Bisbas et al. 2022). The dust temperature we recover for the bulk of the gas in the ADAPTIVEG0 models is systemically slightly below those seen in Milky Way observations of  $T_{\text{dust}} \approx 15 - 20 \text{ K}$  (Marsh et al. 2017). The reason behind this is that in our chemical network so far, we only account for dust heating by EUV and FUV but not by far-infrared radiation (FIR). We discuss this discrepancy further in Sect. 4.3.

### 3.3 Heating rates

We take a representative snapshot from the static  $G_0$  simulation  $\Sigma 010$  and re-run the simulation with the ADAPTIVEG0 module for 0.1 Myr starting from this snapshot. The time of the representative snapshot has been chosen so that its instantaneous SFR is close to the globally averaged SFR at  $t_{\text{SFR}} = 19.8 \text{ Myr}$ . By doing so we obtain the closest possible comparison between the two realisations. In Fig. 14, we show a PDF of  $\Gamma_{\text{PE}}$  measured in the snapshots with static  $G_0$  (orange line) and for the same gas configuration with ADAPTIVEG0 (blue line). The heating due to CR ionisation,  $\Gamma_{\text{CR}}$ , is shown as a dashed green line for comparison. In Appendix E, we show the distribution of  $\Gamma_{\text{CR}}$  in relation to  $\Gamma_{\text{PE}}$ . The gas density structures in the presented

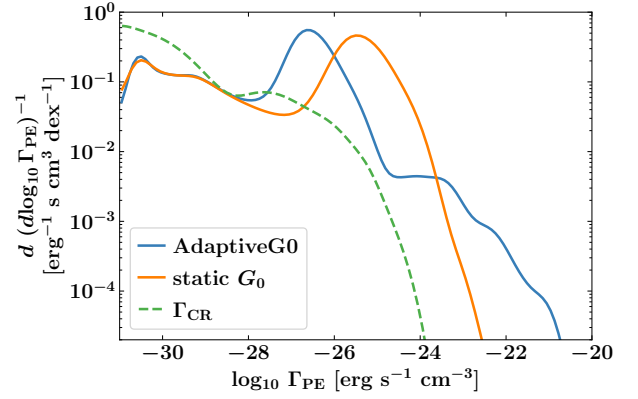


**Figure 14.** Probability density functions of  $\Gamma_{\text{PE}}$  for the cases with ADAPTIVEG0 and static  $G_0$ . The data for this plot was taken from representative snapshots of the  $\Sigma 010$  model around the peak of star formation. We also show the heating caused by CR ionisation,  $\Gamma_{\text{CR}}$  with a dashed green line. The model with a static  $G_0$  field reaches significantly lower maximum  $\Gamma_{\text{PE}}$  values but has the peak of the distribution at higher heating rates than the model with ADAPTIVEG0. CR heating is subordinate to the peak heating rates due to the PE effect on dust grains.

snapshots are close to identical to each other and the differences in the heating rates are due to the differences in the ISRF due to the different treatment of the FUV radiation between ADAPTIVEG0 and static  $G_0$ .

In general,  $\Gamma_{\text{PE}}$  strongly depends on the strength of the FUV radiation field (see Eq. 6). The  $\Gamma_{\text{PE}}$  distribution in Fig. 14 extends nearly 10 orders of magnitude. At the low-energy end of the distribution, the  $\Gamma_{\text{PE}}$  values are virtually identical between both simulations. These  $\Gamma_{\text{PE}}$  correspond regions with the most external and self-shielding. In the ADAPTIVEG0 models, the gas is predominantly exposed to a  $\Gamma_{\text{PE}}$  that is 1.5 to 2 orders of magnitude lower compared to a static  $G_0$  field (see the shift between the peaks of the distributions in Fig. 14). However, for a static  $G_0$ , the amount of gas subjected to high heating rates steeply declines while the ADAPTIVEG0 models reach maximum heating rates of about two orders of magnitude higher than their static counterparts.

To understand how the increased PE heating affects the ISM in star-forming regions, we examine the cumulative volume-filling factor (VFF) of  $\Gamma_{\text{PE}}$  as shown in Fig. 15. We compare the static  $G_0$  model (orange) with the ADAPTIVEG0 model (blue), similar to the comparison in Fig. 14, and plot the cumulative VFF of  $\Gamma_{\text{PE}}$  within the midplane ISM ( $|z| \leq 500 \text{ pc}$ ). Dashed lines indicate the maximum heating rate that affects 90 per cent of the midplane ISM. Despite a significantly higher total energy input in the ADAPTIVEG0 case, most of the gas (90 per cent) experiences a PE heating rate approximately 1.5 dex lower than in the static  $G_0$  model. The excess energy input is concentrated in small volumes near the star cluster sink particles, which are also exposed to hydrogen-ionising EUV radiation and stellar winds. These mechanisms can heat the gas to temperatures exceeding  $T \gtrsim 8 \times 10^3 \text{ K}$ , beyond which even the strongest FUV radiation fields cannot further increase the temperature (see Fig. 6).

We present the time evolution of the effective FUV radiation field energy density available for PE heating,  $e_{\text{eff}} = G_{\text{eff}} \times V \times u_{\text{HAbing}}$ , with gas volume,  $V$ , and  $u_{\text{HAbing}} = 5.29 \times 10^{-14} \text{ erg cm}^{-3}$ , for our models with varying initial  $\Sigma_{\text{gas}}$  in Fig. 16 (top panel), along with the instantaneous volume-averaged midplane  $\Gamma_{\text{PE}}$  (middle panel) and the cumulative thermal energy injected through PE heating (bottom panel). Unlike previous analyses, we include data from before the

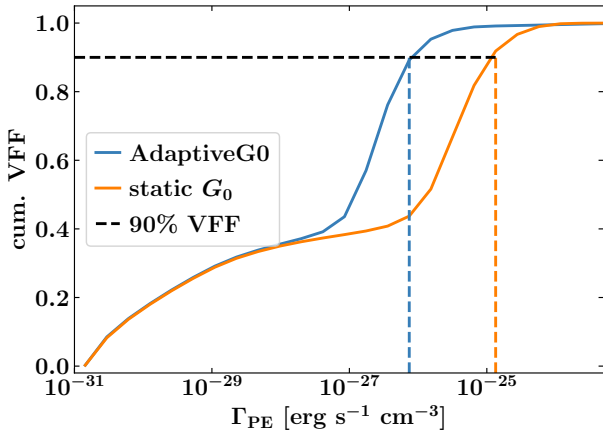


**Figure 15.** Cumulative volume-filling factors, VFF, of  $\Gamma_{\text{PE}}$ , for the case with ADAPTIVEG0 (blue) and static  $G_0$  (orange). We indicate the maximum heating rate to which 90 percent of the midplane ISM volume is exposed (dashed vertical lines). Even though the integrated amount of PE heating for a ADAPTIVEG0 model far exceeds the equivalent energy in a static  $G_0$  model, most of the volume is exposed to lesser PE heating.

onset of star formation,  $t_{\text{SFR}}$ . This inclusion is motivated by the PE heating originating from the static  $G_0$  field independent of star formation in one case, and the heating from the background  $G_{\text{bg}}$  in the other case. The midplane  $e_{\text{eff}}$  is consistently higher in static  $G_0$  models compared to ADAPTIVEG0. Averaged over the full time-evolution and all three  $\Sigma_{\text{gas}}$  models,  $e_{\text{eff}}$  in ADAPTIVEG0 is  $\sim 41 \pm 11$  percent of that in static  $G_0$ . As expected,  $\Gamma_{\text{PE}}$  evolves flat in the static  $G_0$  case with only minor variations due to local changes in the column densities. For the ADAPTIVEG0 models,  $\Gamma_{\text{PE}}$  ramps up drastically with the onset of star formation and strongly varies over time. At higher surface densities ( $\Sigma_{030\text{vFUV}}$  and  $\Sigma_{100\text{vFUV}}$ ), more energy is constantly injected through PE heating than in their corresponding static  $G_0$  counterparts. This demonstrates that PE heating is more efficient in ADAPTIVEG0 models with spatially and temporally varying FUV radiation fields, achieving higher overall energy input despite lower available FUV radiation energy density. For the solar neighbourhood model ( $\Sigma_{010\text{vFUV}}$ ), PE heating injects more energy into the medium during episodes of strong star formation. However, it imparts less thermal energy than the static  $G_0$  model during quiescent periods of star formation. The cumulative energy injected through PE heating (bottom panel of Fig. 16) shows that after the onset of star formation, all models with a self-consistent treatment of the FUV radiation field generated by stellar clusters significantly surpass the energy injection of PE heating in a static model. The difference scales with the system’s initial gas surface density, and therefore with the SFR, and can reach up to three orders of magnitude. However, despite this substantial increase in energy injection into the surroundings of massive star clusters, the overall SFR appears to be unaffected (see Fig. 9 and Fig. 10). FUV photons are absorbed by dust grains in HII regions, but the resulting PE heating is minor compared to the dominant heating from EUV photons ionising hydrogen. The gas in HII regions is mainly heated by the thermalisation of high-energy electrons produced by photoionisation of hydrogen atoms, whereas FUV-driven PE heating becomes more important in the surrounding PDRs where the gas is neutral or only partially ionised.

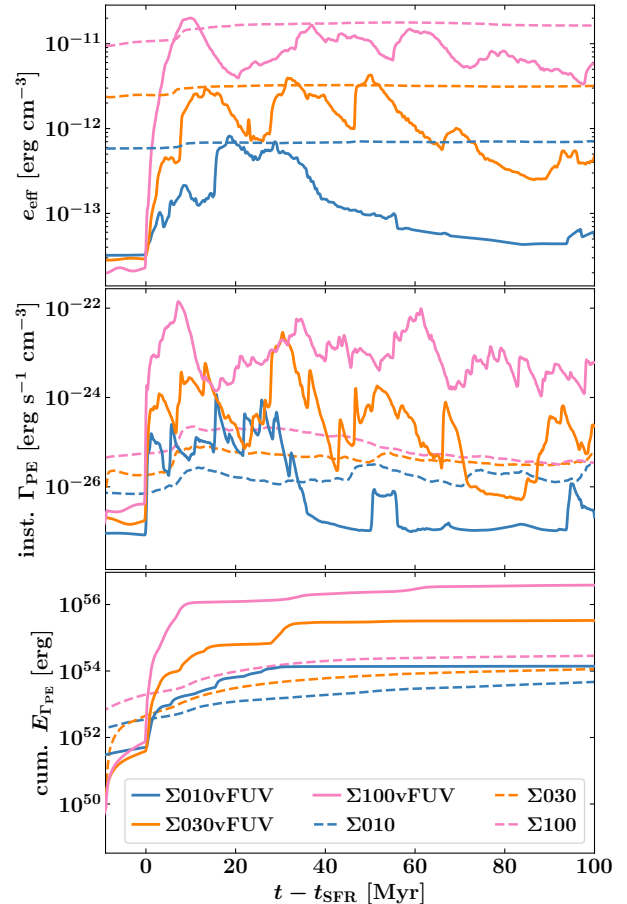


**Figure 16.** *Top:* Effective FUV radiation field energy density,  $e_{\text{eff}} = G_{\text{eff}} \times V \times u_{\text{Habing}}$ , with gas volume,  $V$ , and  $u_{\text{Habing}} = 5.29 \times 10^{-14} \text{ erg cm}^{-3}$ , as a function of time for our different models. We include data from before the onset of star formation since PE heating already takes place during these periods, due to the background ISRF with a strength of either  $G_{\text{bg}}$  or the respective values of the static models (see Table 1). Variations in  $e_{\text{eff}}$  for the static  $G_0$  models arise from varying amounts of shielding experience by the otherwise constant FUV radiation field employed in those models. *Middle:* Instantaneous PE heating rate,  $\Gamma_{\text{PE}}$ . PE heating is more efficient in ADAPTIVEG0 models. *Bottom:* Cumulative energy injected by PE heating,  $E_{\Gamma_{\text{PE}}}$ , over time. The total energy injected into the medium via PE heating for ADAPTIVEG0 models vastly exceeds the corresponding values in the static  $G_0$  models. The amount of PE heating correlates with gas surface density (and therefore also with SFR).

### 3.4 Gas phases

We detail the gas phase distribution in Fig. 17, comparing the full midplane ISM (upper part) and the gas near stellar clusters ( $d < 50 \text{ pc}$ , lower part). The gas is classified into shock-heated hot ionised medium (HIM,  $T > 3 \times 10^5 \text{ K}$ ), WIM ( $300 < T \leq 3 \times 10^5 \text{ K}$ , ionisation parameter  $\chi \geq 0.5$ ), WNM ( $300 < T \leq 3 \times 10^5 \text{ K}$ ,  $\chi < 0.5$ ), and CNM ( $T \leq 300 \text{ K}$ ). The data is presented using box plots similar to Fig. 10, where boxes represent the 25<sup>th</sup> and 75<sup>th</sup> percentiles. The thick horizontal line shows the median and the red dot indicates the mean value over time. Whiskers mark the maximum and minimum values, while shaded areas denote the standard deviation of the mean. The colour-coding represents the initial  $\Sigma_{\text{gas}}$  of the model. In each pair of models with the same  $\Sigma_{\text{gas}}$ , the ADAPTIVEG0 model is on the left and the static  $G_0$  model is on the right. The negligible MFs of the HIM gas phase are not shown. By analysing

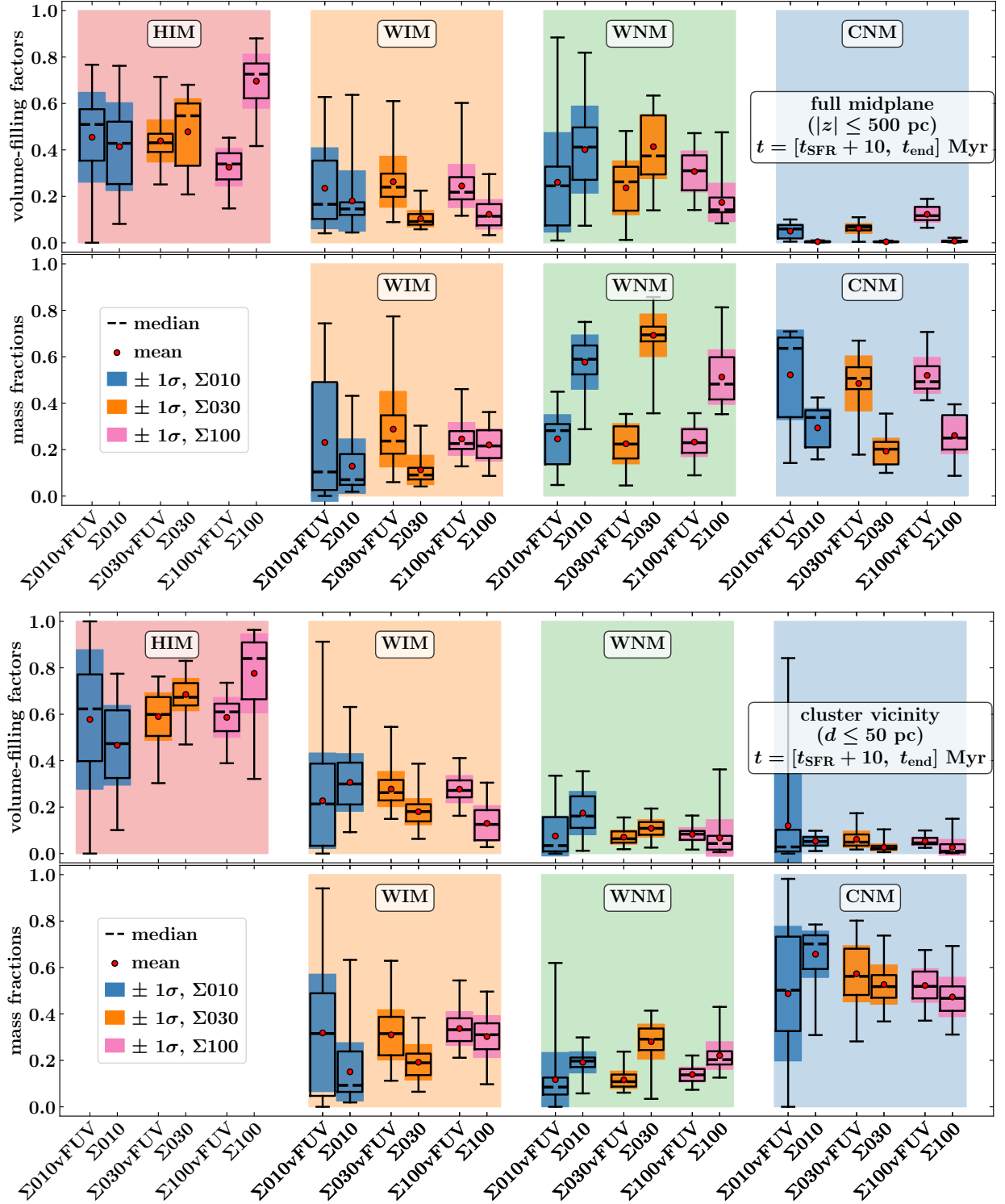


**Figure 17.** *Top figure:* MFs (*top panel*) and VFFs (*bottom panel*) of the hot (HIM,  $T > 3 \times 10^5$  K), warm ionised (WIM,  $300 < T \leq 3 \times 10^5$  K,  $\chi_{\text{ion}} \geq 0.5$ ), warm neutral (WNM,  $300 < T \leq 3 \times 10^5$  K,  $\chi_{\text{ion}} < 0.5$ ), and cold neutral (CNM,  $T \leq 300$  K) gas phases within the midplane ( $|z| \leq 500$  pc). The data is processed in the same way as in Fig. 10 with the median, the 25<sup>th</sup> percentile and 75<sup>th</sup> percentile shown as a box plot, the whiskers indicating the minimum and maximum values and the red dots and shaded area indicating the time-average with  $\pm 1\sigma$  standard deviation. A self-consistent FUV treatment boosts the MFs of the warm neutral and cold gas phases. *Bottom figure:* Same overview of the MF and VFF of the different gas phases as above but this time only considering the gas in the vicinity of the stellar clusters ( $d \leq 50$  pc, same as the used FUV injection radius). Similar trends develop for the WNM in the cluster vicinity compared to the full midplane.

both the full midplane ISM and the vicinity of star clusters, we can better understand how the ISRF influences star formation and the overall chemistry and dynamics of the ISM.

The most striking difference in the midplane ISM is the significant increase in the CNM MF at the expense of the WNM<sup>5</sup>. This increase in the potential molecular CNM aligns with the findings in Sect. 3.2. We measure a significant CNM VFF ranging from VFF = 5 – 12 per cent, scaling with  $\Sigma_{\text{gas}}$ . The absence of artificial PE heating in static  $G_0$  models, particularly in regions distant from massive star clusters, has two significant effects. Firstly, it facilitates increased molecular gas formation. Secondly, it prevents the destruction of diffuse molecular gas that has formed in denser regions and subsequently dispersed, by avoiding excessive heating of this gas. The CRs, modelled as a distinct relativistic fluid using an advection-diffusion approximation, contribute an extra pressure component to the system. This CR pressure, which permeates the ISM, provides further support to the diffuse molecular gas phase, helping it resist compression from external forces and maintain pressure equilibrium.

In Fig. 18, we show the time evolution of the midplane MFs for the different thermal phases. We summarise and quantify the average and median MFs and VFFs in Table A2 and Table A3 in Appendix A. The ADAPTIVEGO simulations have a systematically lower amount of gas in the thermally unstable regime and an increased amount of gas in the CNM throughout the simulated time. However, we also see two deviations of this behaviour with temporary peaks in the WIM MF of the models  $\Sigma 010\text{vFUV}$  and  $\Sigma 030\text{vFUV}$ . The self-consistent FUV radiation field treatment does not cause these outliers, they result from the systems' underlying gas dynamics. While the total stellar mass in each system is an important factor, the individual mass of those stars (determined stochastically by our star formation model) is crucial since more massive stars significantly contribute to photoionisation, which likely sustains the WIM. Additionally, the spatial distribution of the stars strongly impacts the efficiency of stellar feedback. To explain the WIM peaks, we further analyse these aspects in Appendix F.

## 4 DISCUSSION

### 4.1 The impact of far-ultraviolet radiation on star formation in the literature

In the literature, the relative importance of the FUV ISRF for self-regulating star formation is ambiguous. We discuss our findings in the context of the numerical work of other groups.

The closest comparison to our simulation framework can be made with the TIGRESS simulation suite. In the "classic" model (Kim & Ostriker 2017), the multiphase ISM is simulated in a tall-box setup, similar to ours. A major difference to the SILCC PROJECT framework is the inclusion of large-scale galactic rotation realised with a shearing box. This enables them to simulate larger systems over multiple galactic orbits since they can model the impact of the large-scale galactic shearing motions. These large-scale motions, which can efficiently redistribute gravitational energy, have been argued to be another regulatory mechanism for star formation and a driver for ISM turbulence (see e.g. Krumholz et al. 2018), as well as for

<sup>5</sup> We do not employ the use of tracer particles which prohibits us from giving definitive answers about how the gas transitions between the different phases in detail. We can only explain the overall evolution given the integrated quantities.

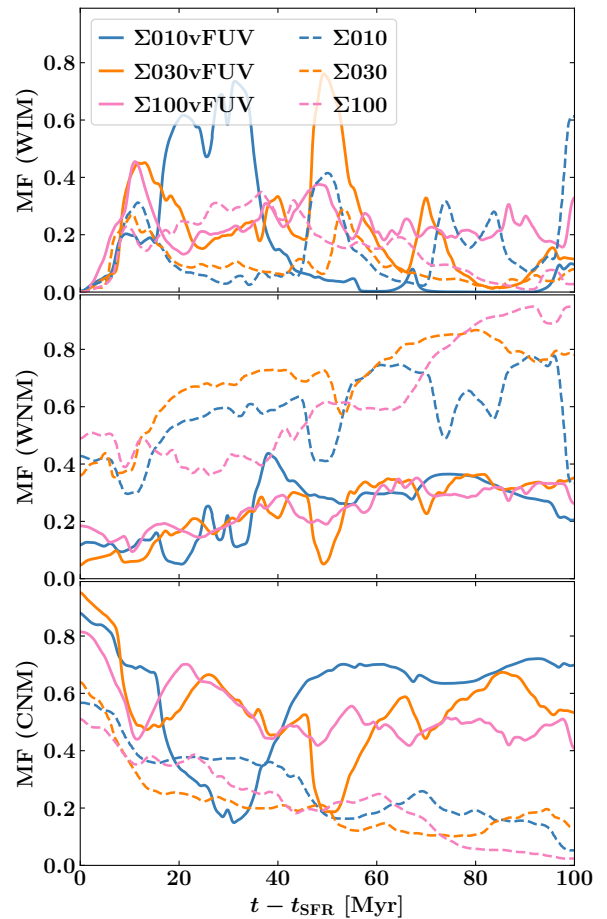


**Figure 18.** Time evolution of the midplane ( $|z| \leq 500$  pc) MFs of the WIM (top), WNM (middle), and CNM (bottom). In ADAPTIVEGO models, the amount of gas in the thermally unstable phase is reduced and added to the CNM. This adjustment leads to a noticeable redistribution of gas phases over time, with the ADAPTIVEGO models showing more pronounced fluctuations in the CNM MF compared to the static  $G_0$  models. The two outlier peaks in the  $\Sigma 010\text{vFUV}$  and  $\Sigma 030\text{vFUV}$  WIM MF are discussed in Appendix F.

large-scale magnetic dynamos (see e.g. Gent et al. 2024). The TIGRESS simulation incorporates stochastically sampled star formation with a sink particle approach. The stellar feedback is realised through SNe and PE heating by a time-dependent ambient FUV field. Their model assumes that  $\Gamma_{\text{PE}} \propto \Sigma_{\text{FUV}} \equiv L_{\text{FUV}}/(L_x L_y)$ . The total FUV luminosity,  $L_{\text{FUV}}$ , is integrated over all present star particles and therefore spatially constant. This will inevitably lead to increased artificial PE heating regions without star formation. They report a  $\Sigma_{\text{SFR}} \approx 5 \times 10^{-3} M_{\odot} \text{ yr}^{-1} \text{ kpc}^{-2}$  for their solar neighbourhood model with an initial  $\Sigma_{\text{gas}} = 13 M_{\odot} \text{ pc}^{-2}$  at  $dx \approx 4$  pc spatial resolution.

In Kim et al. (2023b), the model was updated to TIGRESS-NCR (non-equilibrium cooling and radiation), including the propagation of UV radiation through radiative transfer. This is coupled to a chemical network primarily involving hydrogen and carbon photo-chemistry, which also accounts for CR ionisation (Kim et al. 2023a). TIGRESS-NCR achieves a complexity in photo-chemistry similar to our work presented in Rathjen et al. (2021) but does not account for other stellar feedback mechanisms like stellar winds and the transport of CRs. CR transport, with a focus on its impact on galactic outflows, has been

added to the TIGRESS framework in [Armillotta et al. \(2024\)](#). For radiation propagation, [Kim et al. \(2023b\)](#) implemented a direct ray-tracing method with three energy bands (PE photons, Lyman-Werner photons, and Lyman continuum), which accounts for the attenuation by dust along the rays. In [Kim et al. \(2023b\)](#), two configurations are presented with  $\Sigma_{\text{gas}} = 12 M_{\odot} \text{pc}^{-2}$  and  $\Sigma_{\text{gas}} = 50 M_{\odot} \text{pc}^{-2}$ , respectively. The sources of the UV are the star cluster particles with a mass-weighted age  $t_{\text{age}} < 20 \text{ Myr}$ . This is a good approximation for the EUV but might drastically underpredict the FUV radiation emitted by older low-mass stars. To save computational costs, [Kim et al. \(2023b\)](#) terminate the ray transfer of the FUV above a height of  $|z| = 300 \text{ pc}$  and switch to an analytical plane-parallel assumption from there. They test different limits in the horizontal maximum propagation distance,  $d_{\text{xy}}$  (between 512 pc and 4096 pc), as well as a termination of the FUV radiation transfer when the luminosity of an individually transported photon package becomes lower than the total FUV luminosity in the system times a prefactor,  $\epsilon_{\text{pp}} = 10^{-9}$ – $10^{-7}$ . This FUV efficiency cut-off can lead to an underestimation of the contribution of low-luminosity sources. While these tests of varying propagation distance and FUV cut-off did not achieve convergence in total FUV radiation energy density at larger heights, the computationally motivated parameter choices had minimal impact on the thermal and dynamical balance of the ISM, particularly near the midplane. This result aligns with the assumptions we have made in this study regarding the limited propagation distance of the FUV under consideration of the star-forming capabilities of the midplane ISM.

Their models run for up to 700 Myr, facilitated by the shear-ing box setup. Without this, the galactic context could not be considered, and simulating a galactic patch model over multiple orbit periods would cease to make physical sense. Their analysis is carried out over a 200 Myr time stretch starting approximately 150 Myr after the onset of star formation. Regarding star formation, they observe a median  $\Sigma_{\text{SFR}} (\pm 16^{\text{th}}, 84^{\text{th}} \text{ percentile})$  of  $\Sigma_{\text{SFR}} = [2.8^{+1.5}_{-1.0}, 29.0^{+20.3}_{-8.5}] M_{\odot} \text{yr}^{-1} \text{kpc}^{-2}$ . The gas surface densities during this time frame are  $\Sigma_{\text{gas}} = [10.6^{+0.3}_{-0.2}, 36.2^{+1.4}_{-0.6}] M_{\odot} \text{pc}^{-2}$ . These results are similar to our findings (see [Table A1](#)), which was expected due to their inclusion of non-equilibrium chemistry and ionising radiative transfer. Compared to the results from [Kim & Ostriker \(2017\)](#), which used a simplistic stellar feedback model with only SNe and a planar FUV ISRF scaled by the SFR,  $\Sigma_{\text{SFR}}$  is reduced by roughly a factor of two in the solar neighbourhood model (labelled *R8* in the TIGRESS framework). This is another indicator of the importance of self-consistent early stellar feedback. [Kim et al. \(2023b\)](#) also provide a study of the VFF and MF of the thermal gas phases with a more refined distinction of a total of nine (partly overlapping) phases compared to our four (CNM, WNM, WIM, HIM). For comparison, we group their cold molecular and cold neutral medium as CNM, unstable neutral and warm neutral medium as WNM, warm photoionised, warm collisional ionised and warm-hot ionised medium as WIM, and finally hot ionised as HIM (see [Table 3](#) in [Kim et al. 2023b](#)). Derived from their values in [Table 3](#), we acquire the averaged MF and VFF ( $\pm 1\sigma$ ) of  $\text{MF}_{\text{CNM}}^{\text{KO23}} = 26(\pm 4)$  per cent,  $\text{MF}_{\text{WNM}}^{\text{KO23}} = 65(\pm 9)$  per cent,  $\text{MF}_{\text{WIM}}^{\text{KO23}} = 8(\pm 3)$  per cent,  $\text{VFF}_{\text{CNM}}^{\text{KO23}} = 1.5(\pm 0.4)$  per cent,  $\text{VFF}_{\text{WNM}}^{\text{KO23}} = 65(\pm 7)$  per cent,  $\text{VFF}_{\text{WIM}}^{\text{KO23}} = 16(\pm 4)$  per cent, and  $\text{VFF}_{\text{HIM}}^{\text{KO23}} = 18(\pm 7)$  per cent. The inclusion of self-shielding leads to a higher  $\text{VFF}_{\text{CNM}}^{\text{KO23}}$  in TIGRESS-NCR compared to TIGRESS-classic. Additionally, they see an increase in the  $\text{VFF}_{\text{WIM}}^{\text{KO23}}$  caused by photoionisation. Compared to observational estimates provided in [Tielens \(2005\)](#), the TIGRESS-NCR framework underpredicts the MF of the CNM and the WIM ( $\text{MF}_{\text{CNM}}^{\text{obs}} \approx 48$  per cent,

$\text{MF}_{\text{WIM}}^{\text{obs}} \approx 14$  per cent). Our chemical network and stellar feedback model yield predictions much closer to the observed estimates ( $\text{MF}_{\text{CNM}} = 52(\pm 19)$  per cent, see [Table A2](#)). The spatially and temporally variable FUV ISRF ensures that the thermal balance in the volume-filling warm and cold ISM is self-consistent. Another feature that differs between the TIGRESS and SILCC models is the VFF of the hot ionised gas phase. TIGRESS-NCR predicts  $\text{VFF}_{\text{HIM}}^{\text{KO23}} = 18(\pm 7)$  per cent, while we find  $\text{VFF}_{\text{HIM}} = 45(\pm 19)$  per cent, in closer agreement with observed estimates of  $\text{VFF}_{\text{HIM}}^{\text{obs}} \approx 50$  per cent ([Tielens 2005](#)).

The galactic patch simulations by [Butler et al. \(2017\)](#) use a model with  $\Sigma_{\text{gas}} = 17 M_{\odot} \text{pc}^{-2}$ . This model includes subgrid star formation, supernova feedback, and a moment-method radiative transfer scheme that treats the radiation field as a fluid rather than using explicit ray tracing. They consider four energy bands: one for  $\text{H}_2$ -dissociating Lyman-Werner photons and three for EUV photons, distinguishing the ionisation of helium (He). They systematically toggle different stellar feedback mechanisms on and off and find that in starburst regions,  $\text{H}_2$ -dissociating radiation has the strongest impact on reducing the SFR compared to a model without any feedback. These effects are less pronounced when considering the full kpc-sized domain. However, they do not examine the impact of the EUV radiation band alone, which we argue has the strongest effect on self-regulating star formation. They report that the reduction in  $\Sigma_{\text{SFR}}$  by supernovae is comparable to that by FUV radiation. Nevertheless, the chemical state of the ISM differs significantly between the SN-only and FUV-only runs. They state that models including both the FUV and EUV radiation bands and supernovae match observations best, similar to our claims. For their starburst region with all feedback channels considered, they show an average  $\Sigma_{\text{gas}} \approx 20 M_{\odot} \text{pc}^{-2}$  and  $\Sigma_{\text{SFR}} \approx 3 \times 10^{-2} M_{\odot} \text{yr}^{-1} \text{kpc}^{-2}$ , which is aligned with our  $\Sigma 030\text{vFUV}$  and  $\Sigma 030$  models (average  $\Sigma_{\text{SFR}} = [44 \pm 20, 30 \pm 28] M_{\odot} \text{yr}^{-1} \text{kpc}^{-2}$ , respectively). Only supernovae or only FUV radiation feedback leads to highly elevated SFRs of the order  $10^{-1} M_{\odot} \text{yr}^{-1} \text{kpc}^{-2}$  in that region.

Isolated dwarf galaxy setups are the focus of extensive numerical studies, as they enable high enough resolution (spatial or mass, depending on the code approach) due to their lower total mass (e.g. [Hu et al. 2017](#); [Emerick et al. 2018](#); [Lahén et al. 2019](#); [Sugimura et al. 2024](#)). [Hu et al. \(2017\)](#) studied the effects of a variable ISRF in smoothed particle hydrodynamics (SPH) dwarf galaxy simulations and compared the efficacy of PE heating and supernovae (SNe). Their treatment of the FUV ISRF is similar to ours, integrating the FUV luminosity over all present star particles and accounting for geometric attenuation ( $G_{\text{eff}} \propto R^{-2}$ ) and dust attenuation. Photoionisation is modelled using a Strömgren-sphere approach rather than direct radiative transfer. They arrive at similar conclusions as [Butler et al. \(2017\)](#), finding that PE heating achieves a similar reduction in the SFR as SNe but with a drastically different ISM composition. However, they also emphasise the strong non-linear coupling of different stellar feedback processes, making it impractical or unphysical to rule out the importance of a single feedback channel. We further emphasise that the effects of PE heating, which depend on the hydrogen number density and non-linearly on the electron number density, might be vastly overestimated in models that do not account for stellar winds or the proper propagation of EUV radiation and the development of HII regions around young massive stars. Photoionisation and stellar winds disperse the star-forming environment, leading to a drastic reduction in the ambient density. PE heating appears to be subdominant. Models that do not account for EUV radiation and stellar winds might see a stronger influence of PE heating while also lacking the

formation mechanisms for the WIM. It is thus important to account for all early stellar feedback channels in addition to SNe to achieve a realistic model of the multiphase ISM with locally self-regulated star formation.

The parsec-scale low-mass dwarf galaxy simulations by [Emerick et al. \(2018\)](#) follow detailed stellar feedback on a star-by-star basis and utilise an adaptive ray-tracing radiative transfer method for the ionising radiation, as well as SNe and wind feedback from both young massive stars and asymptotic giant branch (AGB) stars. They assume the FUV radiation to be optically thin with local attenuation, similar to our approach. Similar to [Hu et al. \(2017\)](#) and our findings, [Emerick et al. \(2018\)](#) conclude that multichannel stellar feedback (i.e., early feedback in the form of winds and especially ionising radiation, but also PE heating from FUV radiation plus SNe) is needed to model a realistic evolution of dwarf galaxies. Their simulations agree with observations regarding star formation, galactic outflows, and the overall composition/metallicity of the ISM.

[Smith et al. \(2021\)](#) simulate isolated dwarf galaxies with parsec-scale simulations in which star formation is modelled by explicitly sampling massive stars from an IMF, enabling the modelling of individual HII regions, PE heating from a spatially varying FUV ISRF, and SN feedback. Their PE heating approach, similar to [Hu et al. \(2017, see above\)](#), models the FUV luminosity of each star cluster sink particle, accounting for geometric ( $G_{\text{eff}} \propto R^{-2}$ ) and dust attenuation. Short-range photoionisation is modelled using an overlapping Strömgren-type approach, accounting for anisotropic neutral gas distribution rather than perfectly spherical HII regions. SNe are implemented through thermal energy injection of order  $E_{\text{inj}} = 10^{51}$  erg. [Smith et al. \(2021\)](#) test various combinations of these feedback channels, finding that photoionisation and SNe independently can regulate star formation to the same level, with photoionisation-regulated star formation being less bursty than SN-regulated star formation. PE heating alone is insufficient to regulate star formation to that level. The latter results align well with our findings.

Motivated by recent high-redshift ( $z \gtrsim 8$ ) observations of the first galaxies by JWST, [Sugimura et al. \(2024\)](#) model metal-poor galaxies with a cosmological zoom-in approach that would evolve into a dwarf galaxy analogue in the Local Group by  $z = 0$ . In their study, they focus on the impact of FUV and EUV radiation and distinguish between Pop II and Pop III stars at sub-pc resolution up to a redshift of  $z \approx 10$  while including non-equilibrium chemistry. Their radiative transfer is a moment-based method with M1 closure and allows for four photon energy bins (Lyman-Werner, H-ionising, He-ionising, He<sup>+</sup>-ionising). Interestingly, they find a positive effect of FUV radiation from Pop II stars on the SFR. First, the extremely low-metallicity clouds in the first galaxies are heated to  $\sim 10^4$  K by the diffuse FUV radiation field. This retards star formation and allows the clouds to accumulate more gas. As the clouds become very massive, self-shielding begins to occur. This cools the clouds, which then become gravitationally unstable and trigger rapid star formation because of the large amount of gas available. This effect can also explain the observed bursty star formation and clumpiness in high-redshift galaxies. They find that EUV radiation from Pop II stars is not able to photoevaporate the gas within the first galaxies. However, EUV radiation from Pop III stars can, in turn, enhance the efficiency of the subsequent supernovae. The results from [Sugimura et al. \(2024\)](#) highlight that the effects of various stellar feedback mechanisms are not static for different systems over cosmological time. Changes in overall gas mass and metallicity can strongly impact how efficiently feedback regulates star formation and can even cause a qualitative switch from positive to negative feedback.

A similar conclusion about the impact of metallicity is drawn in [Bialy \(2020\)](#), where an analytical model for the FUV ISRF flux as a function of dust-to-gas ratio,  $\Sigma_{\text{SFR}}$ , gas density, scale radius, and position of the observer is developed and applied to a series of galactic disc simulations. They find that the ISRF flux per  $\Sigma_{\text{SFR}}$  is anti-correlated with the metallicity of the systems, i.e., the  $F_{\text{ISRF}} \Sigma_{\text{SFR}}^{-1}$  is a factor of three to six higher in metal-poor dwarf galaxies than in their Milky Way-like (MW-like) counterparts. Hence, in metal-poor systems, FUV radiation might be the main regulating mechanism of star formation. However, potentially stronger effects of EUV radiation or SNe on the SFR are not taken into account. Nonetheless, these results show that it is important to note that our findings could potentially only apply to systems with solar metallicity and gas surface densities between  $\Sigma_{\text{gas}} = 10 - 100 \text{ M}_{\odot} \text{ pc}^{-2}$ .

The effects of PE heating triggered by FUV radiation on star formation have also been studied in more massive isolated MW-like disc galaxies but at the cost of less sophisticated stellar feedback models. [Tasker \(2011\)](#) modelled kpc-scale disc galaxies with a galactic-radial dependent PE heating rate with an ISRF strength of  $G_0 = 1.7$  and a radial scale length of 8 kpc. They account for tabulated radiative cooling and star formation with fixed star formation efficiency,  $\epsilon_{\text{SF}}$ , but without EUV radiation, stellar winds or SNe. Compared to their no-feedback model, PE heating suppresses cloud fragmentation and reduces star formation. However, they show that their measured SFR is still more than an order of magnitude higher than in observed local neighbourhood galaxies. This is due to the lack of additional stellar feedback processes, especially SNe and ionising radiation.

[Osman et al. \(2020\)](#) use a more refined stellar feedback model in their MW-like isolated disc galaxy simulation and include SNe and PE heating through FUV radiation but still no explicit radiative transfer for hydrogen-ionising radiation. The strength of their FUV radiation field is estimated with a stellar population synthesis code considering the age and metallicity of the stellar particle. In addition, they deploy an extensive dust model which considers the formation and destruction of dust. They can switch the PE heating on and off and vary various model parameters of their dust model. Depending on the choice of parameters, they report suppression of star formation by factors between zero and five. Models with higher gas fractions ( $f_{\text{gas}} \sim 0.5$ ) exhibit a stronger suppression of the SFR. Additionally, they identify a secondary large-scale effect that regulates the SFR. In their models, the effectiveness of SNe is enhanced when PE heating is considered, due to the pre-processing of the gas before the SN explosion. This results in stronger thermally driven ballistic outflows, which deplete the ISM more quickly and subsequently reduce star formation. However, we argue that the dispersion of gas around single stars solely by FUV radiation is likely to be rather small, as demonstrated in [Fig. 5](#). Moreover, EUV radiation is capable of evacuating star-forming regions and enabling SNe to become the most efficient with the least amount of radiative cooling losses (see also [Rathjen et al. 2021](#)).

The FUV ISRF can also be studied in terms of its effects on the thermal phases and stability of the multiphase ISM. Our models demonstrate a clearer separation of respective gas phases and a reduction in thermally unstable gas (see [Sect. 3.2 and 3.4](#)). Accurate modelling of the FUV radiation field is crucial for understanding star formation and the chemical evolution of the ISM. The time- and space-varying nature of the ISRF is particularly important in this context. Our findings indicate an increase in cold neutral gas fractions in models with ADAPTIVEG0, suggesting a higher potential for molecular gas formation in regions shielded from strong FUV radiation. Variations in heating rates and cumulative



energy injection through PE heating significantly impact the ISM's thermodynamic properties. Previous studies, such as Hill et al. (2018) and Bialy (2020), have shown that the FUV ISRF's intensity in galaxies determines the thermal and chemical evolution of neutral interstellar gas and is essential for interpreting extragalactic observations and star formation theories. The isolated galactic disc model with SN feedback and explicit ray-tracing FUV radiation transport (one energy band, PE plus Lyman-Werner photons) by Benincasa et al. (2020) agree with Hu et al. (2017) and our findings that star formation cannot be efficiently regulated via FUV-induced PE heating but that a correct treatment of the FUV ISRF is needed to arrive at realistic ISM phases. However, Benincasa et al. (2020) only account for the thermal balance in the ISM through the direct PE heating by dust grains since they do not model the formation and destruction of molecules. From the observational side, FUV radiation is often used as a tracer for star formation (see e.g. Leroy et al. 2008). A detailed and self-consistent FUV radiation field in numerical simulations allows us to create synthetic observations and further calibrate and inform observational models.

In summary, this study highlights the significant impact of varying ISRF conditions on the ISM's thermodynamic properties and emphasises the necessity of accurately modelling the FUV radiation field to resolve the ISM's gas phases. Nevertheless, the impact of the FUV radiation field on massive star formation is negligible for systems at solar metallicity when also accounting for additional stellar feedback mechanisms. It was demonstrated in Rathjen et al. (2021) that HII regions created by hydrogen-ionising radiation might be the strongest regulator of massive star formation. Another important component in dispersing massive star-forming regions could be the momentum input from wind-blown bubbles of massive stars (see e.g. Weaver et al. 1977). However, this has not yet been convincingly demonstrated in ISM scale experiments, most likely due to lacking numerical resolution (Lancaster et al. 2024).

## 4.2 The diffuse molecular gas

The primary objective of this study is to understand the impact of the FUV ISRF on the star formation efficiency in the ISM. However, a potentially controversial finding emerging from this study is the existence of a cold diffuse molecular gas phase in our ADAPTIVEG0 models, not previously observed in parsec-scale numerical experiments of the star-forming multiphase ISM. This raises the question of whether this cold diffuse gas phase has a physical explanation or is an artefact of our model limitations.

To address this, we analysed the properties of the cold diffuse medium (CDM) based on the  $\Sigma 010vFUV$ ,  $\Sigma 030vFUV$ , and  $\Sigma 100vFUV$  simulations towards the end at  $t - t_{SFR} \approx 60$  Myr. A comprehensive follow-up study focusing solely on the diffuse molecular gas is in preparation.

For any given time step, we define the star-forming plane as the average  $z$ -height of the star cluster sink particles weighted by their current mass. Then we calculate the distance of the diffuse  $H_2$  gas parcels to that plane. We define  $d_{CDM}$  as the mean of those distances, weighted by the mass of each diffuse  $H_2$  gas parcel and find  $d_{CDM} = 162 \pm 62$  pc. This suggests that most of the CDM is located further than  $d = 50$  pc from active star clusters and is thus only irradiated by an ISRF with strength  $G_{bg} = 0.0948$ . However, CDM pockets also exist within the star-forming plane, with overall vertical distances  $z_{CDM}$  ranging from  $\leq 3.9$  pc to  $823 \pm 143$  pc, averaged over the three models with varying initial  $\Sigma_{gas}$ .

The total mass of the CDM ranges between  $M_{CDM} \approx 1.0 - 1.4 \times$

$10^4 M_{\odot}$ , which is insignificant compared to the total gas mass in the midplane ISM ( $\sim 1 - 10 \times 10^6 M_{\odot}$ ). When we assume a free-fall time  $t_{ff} = \sqrt{\frac{3\pi}{32G\rho}}$ , with gravitational constant  $G$  and total gas density,  $\rho$ , for the diffuse  $H_2$  gas with  $n_{H_2} \ll 2 \text{ cm}^{-3}$  (see Fig. 12), we can calculate  $t_{ff}^{CDM} \gtrsim 25$  Myr. This suggests that the CDM is highly unlikely to collapse under its self-gravity.

The thermal pressure in the CDM measured in our simulations is  $\sim 90 \text{ K cm}^{-3}$ . Additional support against the external pressure of the WNM comes from the CR component. The median CR pressure in gas cells below  $\sim 50$  K and with an  $H_2$  number density between  $n_{H_2} = 10^{-5} - 1 \text{ cm}^{-3}$  is approximately four orders of magnitude higher than the thermal pressure in these regimes.

These CRs originate from supernova remnants embedded in the star-forming ISM and diffuse almost freely through the medium, creating a negative CR pressure gradient along the vertical axis of the simulation domain (see e.g. Girichidis et al. 2018a). Their inefficient cooling provides a long-lasting energy reservoir, leading to additional support, especially in diffuse gas. This property also enables CRs to support cold gas galactic outflows, as demonstrated in Rathjen et al. (2023).

## 4.3 Caveats and future improvements

While this study provides valuable insights into the dynamics of the ISM and its interaction with the ISRF, several caveats and areas for future improvement should be considered.

(i) *Simplified radiative transfer approach*: In the ADAPTIVEG0 module, we employ a simplified approach rather than explicit radiative transfer as it is used for ionising radiation with TREERAY/ONTHESPOT (Wünsch et al. 2021). As a first-order approximation, FUV transport does not need iterative radiative transfer as FUV photons do not excite new FUV photon sources when traversing the ISM. However, FUV photons scatter off dust grains while traversing the ISM. Ideally, to treat this scattering properly, each cell should be considered as a potential source of photons.

Our method focuses on calculating the local strength of the ISRF, which is highly dependent on the column density along the line-of-sight and local attenuation. We use the TREERAY/OPTICALDEPTH module (Wünsch et al. 2018), which utilises the HEALPIX algorithm, to calculate this attenuation (see Sect. 2, Eqs. 1 and 4). Due to computational limitations, we cannot store the column densities for each cell and each sightline to a source in the current implementation of the simulation code. Therefore, we calculate and store a 3D-averaged column density for each cell.

Moreover, we limit the FUV photon propagation to  $d = 50$  pc from the emitting stellar source, consistent with our attenuation factor calculation (see Appendix B, for a detailed analysis of this free model parameter). This approach is based on our demonstration in Sect. 2.2 that the strength of the FUV ISRF powered by a single star or massive star cluster is a strong function of distance to the source. However, we recognise that this simplified approach has limitations. Proper treatment of radiation transfer requires knowledge of the attenuation between the source and each cell along each ray. Our approximate method therefore does not model the exact attenuation of the FUV by dust and also does not capture other relevant physics like dust scattering. We acknowledge that explicit full radiative transfer would provide a more accurate treatment of the FUV ISRF.

(ii) *One FUV energy band*: We currently do not consider multiple energy bands for non-ionising FUV photons. As described in Sect. 2, we obtain the FUV luminosity of our star cluster sink particles

from STARBURST99. To do so, we integrate over the energy range of  $5.6 \text{ eV} \leq E_\gamma < 13.6 \text{ eV}$ . A possible distinction could be two energy bands for the FUV:  $5.6 \text{ eV} \leq E_{5,6} < 11.2 \text{ eV}$  and  $11.2 \text{ eV} \leq E_{11,2} < 13.6 \text{ eV}$  (see e.g. [Baczynski et al. 2015](#)). PE heating is expected to be dominated by photons in the  $E_{5,6}$  band in the dense ISM ([Bakes & Tielens 1994](#)). Photodissociation of  $\text{H}_2$  is triggered by excitation of  $\text{H}_2$  with  $E_{11,2}$  band photons (Lyman-Werner band).

Lower energy photons are only able to dissociate  $\text{H}_2$  that is not in the vibrational ground state and are therefore negligible in our modelling ([Glover 2015](#)). The  $\text{H}_2$  gas is shielded from the FUV ISRF through the external column densities as well as through self-shielding. In the current implementation, we assume that the  $\text{H}_2$  photodissociation rate scales with the radiation intensity of the whole FUV band.

Adding more energy bands increases the numerical complexity and cost but would also increase the accuracy of the ADAPTIVEG0 model. To address these limitations and improve the physical accuracy of our simulations, we plan to implement full radiative transfer for the FUV band, among others, by adding additional energy bands explicitly into our backwards-radiative transfer scheme TREERAY in an upcoming iteration of the SILCC PROJECT.

(iii) *Chemical complexity and metallicity:* All simulations presented here are carried out under the assumption of solar metallicity. We do not account for the effects of chemical variations through enrichment by stellar winds, SNe, or galactic inflows of low-metallicity gas. Furthermore, we do not explicitly follow the evolution of dust but assume a constant dust-to-gas MF of one per cent. The interaction of the FUV field with the gas and especially dust is strongly affected by the assumed metallicity and dust-to-gas ratio. As seen in the discussion in Sect. 4, FUV radiation could play a more important role in regulating  $\Sigma_{\text{SFR}}$  in lower metallicity environments. We explore these effects in [Brugaletta et al. \(in prep.\)](#).

(iv) *Radiation pressure on dust and dust heating from the far-infrared radiation:* We account for the radiation pressure exerted on the gas by EUV photons with TREERAY/ONTHESPOT. The radiation pressure on dust grains is mostly exerted by infrared (IR) radiation but also overlaps with the FUV radiation band. It has been demonstrated that radiation pressure on dust by IR radiation from young massive stars can decrease further fragmentation around the star and add to the self-regulation of star formation ([Klepitko et al. 2023](#)).

Furthermore, our chemical network only considers dust heating by EUV and FUV radiation. We do not account for dust heating by the FIR and lower energy photons. This could lead to a slight underprediction of  $T_{\text{dust}}$  for our models. The dust temperature in the bulk of the gas of the ADAPTIVEG0 models is  $T_{\text{dust}} \approx 10 \text{ K}$ , whereas Milky Way observations suggest temperatures of  $T_{\text{dust}} \approx 15 - 20 \text{ K}$  ([Marsh et al. 2017](#)). The impact of this discrepancy is negligible for the objectives of this study since the slightly higher dust temperature would not strongly alter the dynamics of the ISM or its efficacy in forming stars.

A study with a self-consistent treatment of diffuse FUV radiation in combination with diffuse IR radiation is in planning.

## 5 CONCLUSION

We presented a series of nine magnetohydrodynamic simulations<sup>6</sup> of the multiphase interstellar medium (ISM) in varying galactic environments. The presented simulations are carried out within the SILCC PROJECT simulation framework. Five of the simulations utilise the novel ADAPTIVEG0 module for a self-consistent treatment of the spatially and temporally varying far-ultraviolet interstellar radiation field (FUV ISRF) that is powered by the stellar component. Our primary focus was on understanding how a self-consistent, variable FUV radiation field influences the formation of massive stars, chemical composition, and dust properties in a stratified galactic ISM patch. The main findings of our study are as follows:

(i) **Impact of FUV Radiation on Star Formation:** The simulations show that while FUV radiation can reach local intensities up to  $G_0 \approx 10^4$  (in Habing units), its overall impact on regulating star formation is minor compared to other stellar feedback mechanisms, such as ionising UV radiation, stellar winds, and supernovae. Both static and adaptive FUV radiation fields result in similar SFRs, indicating that the presence of FUV radiation alone does not significantly alter the star formation rate (SFR). At solar neighbourhood conditions, the star formation rate surface densities,  $\Sigma_{\text{SFR}}$ , only vary marginally between the model with ADAPTIVEG0,  $\Sigma_{\text{SFR}} = (5.0 \pm 4.9) \times 10^{-3} \text{ M}_\odot \text{ yr}^{-1} \text{ kpc}^{-2}$  (mean $\pm 1\sigma$ ), and with a simple static FUV radiation field,  $\Sigma_{\text{SFR}} = (4.3 \pm 3.1) \times 10^{-3} \text{ M}_\odot \text{ yr}^{-1} \text{ kpc}^{-2}$  (mean $\pm 1\sigma$ ). The models with only SN feedback or with SNe and the FUV treatment but without stellar winds and ionising radiation ( $\Sigma 010\text{vFUV}\dagger$  and  $\Sigma 010\dagger$ ), exhibit an order of magnitude higher SFR but without a significant difference between them. Their  $\Sigma_{\text{SFR}}$  is  $(35 \pm 2.4) \times 10^{-3} \text{ M}_\odot \text{ yr}^{-1} \text{ kpc}^{-2}$  and  $(33 \pm 2.0) \times 10^{-3} \text{ M}_\odot \text{ yr}^{-1} \text{ kpc}^{-2}$ , respectively. A model at solar neighbourhood conditions without any feedback but with ADAPTIVEG0 ( $\Sigma 010\text{vFUVnoSN}\dagger$ ) shows an average  $\Sigma_{\text{SFR}}$  approximately three times higher, around  $\Sigma_{\text{SFR}} \approx 10^{-2} \text{ M}_\odot \text{ yr}^{-1} \text{ kpc}^{-2}$ . In this model, star formation is only weakly regulated. A measurable difference between the two models is the standard deviation  $\Sigma_{\text{SFR}}$ ,  $\sigma_{\text{SFR}}$ , which can be interpreted as a tracer of the burstiness as star formation. For ADAPTIVEG0 models,  $\sigma_{\text{SFR}}$  decreases to  $87 \pm 44$  per cent ( $62 \pm 32$  per cent without  $\Sigma 010$  simulations) as compared to the static  $G_0$  realisations.

(ii) **Heating Rates:** Photoelectric (PE) heating rates in the ADAPTIVEG0 models show a wider distribution compared to static  $G_0$  models, featuring higher peak rates but lower heating rates across most of the ISM volume. The cumulative energy injected by PE heating in the ADAPTIVEG0 models significantly exceeds that in static models, particularly in regions close to star clusters hosting young massive stars. PE heating is more efficient in ADAPTIVEG0 models as it can reach higher overall heating rates with less overall available FUV radiation energy density for PE heating. In the direct comparison between the two cases for nearly identical gas density structures, we see that the increase in PE heating energy results from the locally significantly higher FUV radiation field (see Sect. 3.3). Less gas further away from active star-forming regions is artificially exposed to extensive PE heating as it would be in the static case. This has implications for the chemical

<sup>6</sup> As mentioned in Sect. 2.3, three out of the total nine simulations presented here have been previously published in [Rathjen et al. \(2023\)](#) and one in [Rathjen et al. \(2021\)](#).

composition of the gas in the midplane ISM and especially on the gas' ability to form and sustain a cold neutral gas medium (CNM).

(iii) **Chemical Properties:** The space- and time-varying FUV radiation field promotes the formation of a diffuse molecular hydrogen gas phase and increases the mass fraction (MF) of the CNM outside the vicinity of stellar clusters. A detailed analysis of the temperature-density phase diagrams reveals that the variable FUV field broadens the equilibrium states of the gas phases, particularly promoting the presence of cold, diffuse gas. This diffuse molecular gas phase is supported against compression from external pressure by the additional cosmic ray pressure component. The MF of the diffuse molecular gas (compared to the total H<sub>2</sub> gas mass) in the ADAPTIVEG0 models is  $22.5 \pm 7.1$  per cent. We measure a systematic reduction of the MF in the warm neutral medium (WNM) by  $36 \pm 6$  percentage points, independent of the initial gas surface density,  $\Sigma_{\text{gas}}$ . At the same time, the CNM MF systematically increases by  $27 \pm 5$  percentage points. We also measure an increase in the warm ionised medium (WIM) by  $8 \pm 6$  percentage points, driven mainly by the increase of the WIM MF in the runs  $\Sigma 010vFUV$  and  $\Sigma 030vFUV$ . We explain this behaviour further in Appendix F.

Furthermore, we detect a significant volume-filling fraction (VFF) of the CNM in the ADAPTIVEG0 models which range from VFF = 5 – 12 per cent, scaling with the initial  $\Sigma_{\text{gas}}$ . Overall, with the self-consistent treatment of the FUV radiation field, we achieve a much clearer separation of the thermal gas phases and observe less thermally unstable gas, both in mass and volume.

## ACKNOWLEDGEMENTS

TER, SW, and DS thank the Deutsche Forschungsgemeinschaft (DFG) for funding through SFB 1601 "HABITATS OF MASSIVE STARS ACROSS COSMIC TIME". TER, SW, and DS further acknowledge support by the project "NRW-Cluster for data-intensive radio astronomy: Big Bang to Big Data (B3D)" funded through the programme "Profilbildung 2020", an initiative of the Ministry of Culture and Science of the State of North Rhine-Westphalia. The sole responsibility for the content of this publication lies with the authors. TN acknowledges the support of the Deutsche Forschungsgemeinschaft (DFG, German Research Foundation) under Germany's Excellence Strategy - EXC-2094 - 390783311 of the DFG Cluster of Excellence "ORIGINS". RW acknowledges the support of the institutional project of the Czech Science Foundation, RVO:67985815. SCOG acknowledges financial support from the European Research Council via the ERC Synergy Grant "ECOGAL" (project ID 855130) and from the Heidelberg Cluster of Excellence (EXC 2181 - 390900948) "STRUCTURES", funded by the German Excellence Strategy. The authors gratefully acknowledge the Gauss Centre for Supercomputing e.V. (www.gauss-centre.eu) for funding this project by providing computing time through the GCS Supercomputer JUWELS at Jülich Supercomputing Centre (JSC).

*Software:* The software used in this work was in part developed by the DOE NNSA-ASC OASCR Flash Centre at the University of Rochester (Fryxell et al. 2000; Dubey et al. 2009). We used STARBURST99 (Leitherer et al. 1999). The simulation results were visualised in part using the YT (Turk et al. 2011), NUMPY (van der Walt et al. 2011), MATPLOTLIB (Hunter 2007), H5PY (Collette et al. 2020), IPYTHON (Perez & Granger 2007).

## DATA AVAILABILITY

The derived data underlying this article will be shared on reasonable request to the corresponding author. The simulation data will be made available on the SILCC PROJECT data web page: <http://silcc.mpa-garching.mpg.de/>.

## REFERENCES

- Agertz O., Kravtsov A. V., Leitner S. N., Gnedin N. Y., 2013, *ApJ*, 770, 25  
 Agertz O., et al., 2020, *MNRAS*, 491, 1656  
 Ali A. A., Harries T. J., 2019, *MNRAS*, 487, 4890  
 Andersson E. P., Mac Low M.-M., Agertz O., Renaud F., Li H., 2024, *A&A*, 681, A28  
 Armillotta L., Ostriker E. C., Kim C.-G., Jiang Y.-F., 2024, *ApJ*, 964, 99  
 Baczynski C., Glover S. C. O., Klessen R. S., 2015, *MNRAS*, 454, 380  
 Bakes E. L. O., Tielens A. G. G. M., 1994, *ApJ*, 427, 822  
 Benincasa S. M., Wadsley J. W., Couchman H. M. P., Pettitt A. R., Keller B. W., Woods R. M., Grond J. J., 2020, *MNRAS*, 499, 2028  
 Bergin E. A., Hartmann L. W., Raymond J. C., Ballesteros-Paredes J., 2004, *ApJ*, 612, 921  
 Bialy S., 2020, *ApJ*, 903, 62  
 Bisbas T. G., Tan J. C., Tanaka K. E. I., 2021, *MNRAS*, 502, 2701  
 Bisbas T. G., et al., 2022, *ApJ*, 934, 115  
 Bouchut F., Klingenberg C., Waagan K., 2007, *Numer. Math.*, 108, 7  
 Butler M. J., Tan J. C., Teyssier R., Rosdahl J., Van Loo S., Nickerson S., 2017, *ApJ*, 841, 82  
 Calzetti D., Armus L., Bohlin R. C., Kinney A. L., Koornneef J., Storchi-Bergmann T., 2000, *ApJ*, 533, 682  
 Clark P. C., Glover S. C. O., Klessen R. S., 2012, *MNRAS*, 420, 745  
 Collette A., et al., 2020, h5py/h5py: 3.1.0, doi:10.5281/zenodo.4250762  
 Dinnbier F., Walch S., 2020, *MNRAS*, 499, 748  
 Draine B. T., 1978, *ApJ Suppl. Ser.*, 36, 595  
 Draine B. T., Bertoldi F., 1996, *ApJ*, 468, 269  
 Dubey A., Antypas K., Ganapathy M. K., Reid L. B., Riley K., Sheeler D., Siegel A., et al., 2009, *Parallel Comput.*, 35, 512  
 Ekström S., Georgy C., Eggenberger P., Meynet G., Mowlavi N., Wyttenbach A., Granada A., et al., 2012, *A&A*, 537, A146  
 Emerick A., Bryan G. L., Mac Low M.-M., 2018, *ApJ*, 865, L22  
 Ferrière K. M., 2001, *Rev. Mod. Phys.*, 73, 1031  
 Forbes J. C., Krumholz M. R., Goldbaum N. J., Dekel A., 2016, *Nature*, 535, 523  
 Fotopoulou C. M., et al., 2024, *MNRAS*, 534, 215  
 Fryxell B., Olson K., Ricker P., Timmes F. X., Zingale M., Lamb D. Q., MacNeice P., et al., 2000, *ApJ Suppl. Ser.*, 131, 273  
 Gatto A., Walch S., Mac Low M.-M., Naab T., Girichidis P., Glover S. C. O., Wünsch R., et al., 2015, *MNRAS*, 449, 1057  
 Gatto A., Walch S., Naab T., Girichidis P., Wünsch R., Glover S. C. O., Klessen R. S., et al., 2017, *MNRAS*, 466, 1903  
 Gent F. A., Mac Low M.-M., Korpi-Lagg M. J., 2024, *ApJ*, 961, 7  
 Girichidis P., et al., 2016, *MNRAS*, 456, 3432  
 Girichidis P., Naab T., Hanasz M., Walch S., 2018a, *MNRAS*, 479, 3042  
 Girichidis P., Seifried D., Naab T., Peters T., Walch S., Wünsch R., Glover S. C. O., et al., 2018b, *MNRAS*, 480, 3511  
 Girichidis P., et al., 2020, *Space Sci. Rev.*, 216, 68  
 Glover S. C. O., 2015, *MNRAS*, 451, 2082  
 Glover S. C. O., Clark P. C., 2012, *MNRAS*, 421, 116  
 Glover S. C. O., Mac Low M.-M., 2007, *ApJ Suppl. Ser.*, 169, 239  
 Glover S. C. O., Federrath C., Mac Low M. M., Klessen R. S., 2010, *MNRAS*, 404, 2  
 Goldsmith P. F., 2001, *ApJ*, 557, 736  
 Goldsmith P. F., Langer W. D., 1978, *ApJ*, 222, 881  
 Haardt F., Madau P., 2012, *ApJ*, 746, 125  
 Haid S., Walch S., Seifried D., Wünsch R., Dinnbier F., Naab T., 2018, *MNRAS*, 478, 4799  
 Haid S., Walch S., Seifried D., Wünsch R., Dinnbier F., Naab T., 2019, *MNRAS*, 482, 4062

Heays A. N., Bosman A. D., van Dishoeck E. F., 2017, *A&A*, 602, A105

Hill A. S., Mac Low M.-M., Gatto A., Ibáñez-Mejía J. C., 2018, *ApJ*, 862, 55

Hollenbach D. J., Tielens A. G. G. M., 1999, *Reviews of Modern Physics*, 71, 173

Hu C.-Y., Naab T., Glover S. C. O., Walch S., Clark P. C., 2017, *MNRAS*, 471, 2151

Hu C.-Y., Schrubba A., Sternberg A., van Dishoeck E. F., 2022, *ApJ*, 931, 28

Hunter J. D., 2007, *Comput. Sci. Eng.*, 9, 90

Kennicutt R. C., 1998, *ApJ*, 498, 541

Kim C.-G., Ostriker E. C., 2017, *ApJ*, 846, 133

Kim C.-G., Kim W.-T., Ostriker E. C., 2011, *ApJ*, 743, 25

Kim J.-G., Gong M., Kim C.-G., Ostriker E. C., 2023a, *ApJ Suppl. Ser.*, 264, 10

Kim C.-G., Kim J.-G., Gong M., Ostriker E. C., 2023b, *ApJ*, 946, 3

Klepitchko A., Walch S., Wunsch R., Seifried D., Dinnbier F., Haid S., 2023, *MNRAS*, 521, 160

Kroupa P., 2001, *MNRAS*, 322, 231

Krumholz M. R., Burkhardt B., Forbes J. C., Crocker R. M., 2018, *MNRAS*, 477, 2716

Lahén N., Naab T., Johansson P. H., Elmegreen B., Hu C.-Y., Walch S., 2019, *ApJ*, 879, L18

Lancaster L., Ostriker E. C., Kim C.-G., Kim J.-G., Bryan G. L., 2024, *ApJ*, 970, 18

Lee H. H., Herbst E., Pineau des Forets G., Roueff E., Le Bourlot J., 1996, *A&A*, 311, 690

Leitherer C., et al., 1999, *ApJS*, 123, 3

Leroy A. K., Walter F., Brinks E., Bigiel F., De Blok W. J. G., Madore B., Thornley M. D., 2008, *Astron. J.*, 136, 2782

Marsh K. A., et al., 2017, *MNRAS*, 471, 2730

McKee C. F., 1989, *ApJ*, 345, 782

Naab T., Ostriker J. P., 2017, *Annu. Rev. A&A*, 55, 59

Nelson R. P., Langer W. D., 1997, *ApJ*, 482, 796

Osman O., Bekki K., Cortese L., 2020, *MNRAS*, 498, 2075

Ossenkopf V., Röllig M., Neufeld D. A., Pilleri P., Lis D. C., Fuente A., van der Tak F. F. S., Bergin E., 2013, *A&A*, 550, A57

Ostriker E. C., McKee C. F., Leroy A. K., 2010, *ApJ*, 721, 975

Perez F., Granger B. E., 2007, *Comput. Sci. Eng.*, 9, 21

Peters T., Naab T., Walch S., Glover S. C. O., Girichidis P., Pellegrini E., Klessen R. S., et al., 2017, *MNRAS*, 466, 3293

Pound M. W., Wolfire M. G., 2023, *AJ*, 165, 25

Rathjen T.-E., Naab T., Girichidis P., Walch S., Wunsch R., Dinnbier F., Seifried D., et al., 2021, *MNRAS*, 504, 1039

Rathjen T.-E., Naab T., Walch S., Seifried D., Girichidis P., Wunsch R., 2023, *MNRAS*, 522, 1843

Röllig M., et al., 2007, *A&A*, 467, 187

Schinnerer E., Leroy A. K., 2024, *ARA&A*, 62, 369

Smith M. C., Bryan G. L., Somerville R. S., Hu C. Y., Teyssier R., Burkhardt B., Hernquist L., 2021, *MNRAS*, 506, 3882

Sugimura K., Ricotti M., Park J., Garcia F. A. B., Yajima H., 2024, *ApJ*, 970, 14

Tasker E. J., 2011, *ApJ*, 730, 11

Tielens A. G., 2005, *The physics and chemistry of the interstellar medium*. Cambridge University Press, doi:10.1017/cbo9780511819056

Tress R. G., Smith R. J., Sormani M. C., Glover S. C. O., Klessen R. S., Mac Low M.-M., Clark P. C., 2020, *MNRAS*, 492, 2973

Turk M. J., Smith B. D., Oishi J. S., Skory S., Skillman S. W., Abel T., Norman M. L., 2011, *ApJ Suppl. Ser.*, 192, 9

Waagan K., Federrath C., Klingenberg C., 2011, *J. Comput. Phys.*, 230, 3331

Walch S. K., Whitworth A. P., Bisbas T., Wunsch R., Hubber D., 2012, *MNRAS*, 427, 625

Walch S., Girichidis P., Naab T., Gatto A., Glover S. C. O., Wunsch R., Klessen R. S., et al., 2015, *MNRAS*, 454, 238

Weaver R., McCray R., Castor J., Shapiro P., Moore R., 1977, *ApJ*, 218, 377

Wolfire M. G., Hollenbach D., McKee C. F., Tielens A. G. G. M., Bakes E. L. O., 1995, *ApJ*, 443, 152

Wolfire M. G., McKee C. F., Hollenbach D., Tielens A. G. G. M., 2003, *ApJ*, 587, 278

**Table A1.** Star formation rate surface density,  $\Sigma_{\text{SFR}}$ , in our models. FUV radiation from young massive stars seems to be negligible for self-regulating  $\Sigma_{\text{SFR}}$ .

	median	mean	$1\sigma$
	[ $\times 10^{-3} M_{\odot} \text{ yr}^{-1} \text{ kpc}^{-2}$ ]		
$\Sigma 10\text{vFUV}$	$3.1^{10}_{0.6}$	5.0	4.9
$\Sigma 30\text{vFUV}$	$43^{62}_{27}$	44	20
$\Sigma 100\text{vFUV}$	$240^{294}_{182}$	240	59
$\Sigma 10$	$3.4^{7.2}_{1.6}$	4.3	3.1
$\Sigma 30$	$21^{36}_{12}$	30	28
$\Sigma 100$	$340^{540}_{110}$	340	220
$\Sigma 10\text{vFUV}\dagger$	$34^{57}_{10}$	35	24
$\Sigma 10\dagger$	$34^{50}_{14}$	33	20
$\Sigma 10\text{vFUVnoSN}\dagger$	$93^{10}_{70}$	90	26

Wünsch R., Walch S., Dinnbier F., Whitworth A. P., 2018, *MNRAS*, 475, 3393

Wünsch R., Walch S., Dinnbier F., Seifried D., Haid S., Klepitchko A., Whitworth A. P., et al., 2021, *MNRAS*, 505, 3730

van Dishoeck E. F., Black J. H., 1988, *ApJ*, 334, 771

van der Walt S., Colbert S. C., Varoquaux G., 2011, *Comput. Sci. Eng.*, 13, 22

## APPENDIX A: TABULATED SUMMARY

In Table A1, we summarise  $\Sigma_{\text{SFR}}$ . The data is calculated for a time range of  $t - t_{\text{SFR}} = [10 : 100]$  Myr. We discard the first 10 Myr after the onset of star formation to reduce the artificial impact due to the initial conditions of the simulations. In the first data column, we quote the median value with the 75<sup>th</sup> percentile and 25<sup>th</sup> percentile as upper and lower bounds. In the second and third data columns, we quote the time-averaged mean and the standard deviation of the mean, respectively. All values are given in units  $10^{-3} M_{\odot} \text{ yr}^{-1} \text{ kpc}^{-2}$ . We present the long-term evolution of the solar neighbourhood models in Appendix D.

We give a quantitative overview of the midplane MF and VFF of the different gas phases in Table A2 and A3, respectively. Models without hydrogen-ionising radiation do not manage to generate a WIM. The CNM in ADAPTIVEG0 models is elevated due to less artificial  $\text{H}_2$  dissociation and PE heating far away from star cluster (sink particles). Remarkably, we can detect a non-zero midplane VFF of the CNM which scales with the initial  $\Sigma_{\text{gas}}$  in the AdaptiveG0 models.

## APPENDIX B: CHOICE FOR THE MAXIMUM DISTANCE OF THE FUV FIELD CALCULATION

The maximum distance,  $d$ , for which a star cluster can affect a cell with its FUV radiation is a free parameter of our model. This distance is equal to the maximum distance for which we calculate the 3D-averaged hydrogen column densities,  $N_{\text{H,tot}}$ , using the TREERAY/OPTICALDEPTH routine (Wünsch et al. 2018), which is based on TREECOL (Clark et al. 2012). We argue that the same distance limits should be used for calculating the column densities and for the cells affected by a star's ISRF because the effective

**Table A2.** Midplane ( $|z| \leq 500$  pc) MFs of the individual thermal gas phases during  $t = [t_{\text{SFR}} + 10, t_{\text{end}}]$  Myr.

	HIM		WIM		WNM		CNM	
	median <sup>75%ile</sup> <sub>25%ile</sub>	mean( $\pm 1\sigma$ )	median <sup>75%ile</sup> <sub>25%ile</sub>	mean( $\pm 1\sigma$ )	median <sup>75%ile</sup> <sub>25%ile</sub>	mean( $\pm 1\sigma$ )	median <sup>75%ile</sup> <sub>25%ile</sub>	mean( $\pm 1\sigma$ )
$\Sigma 10\text{vFUV}$	0.1 <sup>0.2</sup> <sub>0.1</sub>	0.1( $\pm 0.1$ )	10 <sup>49</sup> <sub>3</sub>	23( $\pm 25$ )	28 <sup>31</sup> <sub>14</sub>	25( $\pm 10$ )	64 <sup>68</sup> <sub>34</sub>	52( $\pm 19$ )
$\Sigma 030\text{vFUV}$	0.2 <sup>0.2</sup> <sub>0.1</sub>	0.2( $\pm 0.1$ )	24 <sup>35</sup> <sub>18</sub>	29( $\pm 16$ )	22 <sup>30</sup> <sub>16</sub>	23( $\pm 9$ )	51 <sup>55</sup> <sub>46</sub>	49( $\pm 12$ )
$\Sigma 100\text{vFUV}$	0.2 <sup>0.2</sup> <sub>0.1</sub>	0.2( $\pm 0.1$ )	23 <sup>18</sup> <sub>20</sub>	25( $\pm 7$ )	23 <sup>29</sup> <sub>19</sub>	23( $\pm 6$ )	49 <sup>56</sup> <sub>46</sub>	52( $\pm 8$ )
$\Sigma 10$	0.1 <sup>0.1</sup> <sub>0.1</sub>	0.1( $\pm 0.1$ )	7 <sup>18</sup> <sub>5</sub>	13( $\pm 12$ )	59 <sup>65</sup> <sub>52</sub>	58( $\pm 12$ )	34 <sup>37</sup> <sub>21</sub>	29( $\pm 8$ )
$\Sigma 030$	0.2 <sup>0.3</sup> <sub>0.1</sub>	0.2( $\pm 0.1$ )	9 <sup>49</sup> <sub>7</sub>	11( $\pm 6$ )	69 <sup>73</sup> <sub>67</sub>	69( $\pm 9$ )	20 <sup>23</sup> <sub>14</sub>	19( $\pm 6$ )
$\Sigma 100$	0.7 <sup>0.9</sup> <sub>0.4</sub>	0.7( $\pm 0.3$ )	22 <sup>35</sup> <sub>16</sub>	22( $\pm 7$ )	48 <sup>60</sup> <sub>42</sub>	51( $\pm 12$ )	25 <sup>35</sup> <sub>20</sub>	26( $\pm 8$ )
$\Sigma 10\text{vFUV}\dagger$	0.4 <sup>0.6</sup> <sub>0.3</sub>	0.4( $\pm 0.1$ )	0.9 <sup>1.2</sup> <sub>0.7</sub>	0.9( $\pm 0.3$ )	26 <sup>32</sup> <sub>20</sub>	26( $\pm 7$ )	73 <sup>79</sup> <sub>67</sub>	73( $\pm 7$ )
$\Sigma 10\dagger$	0.6 <sup>0.9</sup> <sub>0.5</sub>	0.7( $\pm 0.3$ )	1.1 <sup>1.3</sup> <sub>1.0</sub>	1.1( $\pm 0.2$ )	33 <sup>35</sup> <sub>32</sub>	34( $\pm 4$ )	65 <sup>67</sup> <sub>63</sub>	65( $\pm 4$ )
$\Sigma 10\text{vFUVnoSN}\dagger$	0.1 <sup>0.1</sup> <sub>0.1</sub>	0.1( $\pm 0.0$ )	0.0 <sup>0.0</sup> <sub>0.0</sub>	0.0( $\pm 0.0$ )	33 <sup>35</sup> <sub>26</sub>	31( $\pm 5$ )	67 <sup>74</sup> <sub>64</sub>	69( $\pm 5$ )

**Table A3.** Midplane ( $|z| \leq 500$  pc) VFFs of the individual thermal gas phases during  $t = [t_{\text{SFR}} + 10, t_{\text{end}}]$  Myr.

	HIM		WIM		WNM		CNM	
	median <sup>75%ile</sup> <sub>25%ile</sub>	mean( $\pm 1\sigma$ )	median <sup>75%ile</sup> <sub>25%ile</sub>	mean( $\pm 1\sigma$ )	median <sup>75%ile</sup> <sub>25%ile</sub>	mean( $\pm 1\sigma$ )	median <sup>75%ile</sup> <sub>25%ile</sub>	mean( $\pm 1\sigma$ )
$\Sigma 10\text{vFUV}$	51 <sup>58</sup> <sub>35</sub>	45( $\pm 19$ )	17 <sup>35</sup> <sub>10</sub>	23( $\pm 17$ )	25 <sup>33</sup> <sub>7</sub>	26( $\pm 21$ )	6 <sup>8</sup> <sub>2</sub>	5( $\pm 3$ )
$\Sigma 030\text{vFUV}$	43 <sup>47</sup> <sub>39</sub>	44( $\pm 9$ )	24 <sup>30</sup> <sub>20</sub>	26( $\pm 11$ )	26 <sup>33</sup> <sub>14</sub>	24( $\pm 12$ )	7 <sup>7</sup> <sub>5</sub>	6( $\pm 2$ )
$\Sigma 100\text{vFUV}$	34 <sup>39</sup> <sub>27</sub>	33( $\pm 8$ )	22 <sup>28</sup> <sub>19</sub>	24( $\pm 9$ )	31 <sup>38</sup> <sub>23</sub>	31( $\pm 9$ )	12 <sup>15</sup> <sub>10</sub>	12( $\pm 3$ )
$\Sigma 10$	43 <sup>52</sup> <sub>25</sub>	41( $\pm 19$ )	15 <sup>17</sup> <sub>12</sub>	18( $\pm 13$ )	41 <sup>50</sup> <sub>27</sub>	40( $\pm 19$ )	0.5 <sup>0.7</sup> <sub>0.3</sub>	0.5( $\pm 0.2$ )
$\Sigma 030$	55 <sup>60</sup> <sub>33</sub>	48( $\pm 14$ )	9 <sup>12</sup> <sub>8</sub>	10( $\pm 4$ )	37 <sup>55</sup> <sub>29</sub>	41( $\pm 14$ )	0.4 <sup>0.5</sup> <sub>0.4</sub>	0.4( $\pm 0.1$ )
$\Sigma 100$	73 <sup>77</sup> <sub>62</sub>	70( $\pm 12$ )	11 <sup>17</sup> <sub>8</sub>	12( $\pm 6$ )	14 <sup>19</sup> <sub>13</sub>	17( $\pm 8$ )	0.6 <sup>0.9</sup> <sub>0.4</sub>	0.7( $\pm 0.4$ )
$\Sigma 10\text{vFUV}\dagger$	89 <sup>92</sup> <sub>83</sub>	88( $\pm 5$ )	3 <sup>4</sup> <sub>2</sub>	3( $\pm 1$ )	7 <sup>11</sup> <sub>4</sub>	8( $\pm 3$ )	1 <sup>2</sup> <sub>1</sub>	1( $\pm 1$ )
$\Sigma 10\dagger$	95 <sup>96</sup> <sub>92</sub>	93( $\pm 4$ )	1 <sup>2</sup> <sub>1</sub>	2( $\pm 1$ )	4 <sup>5</sup> <sub>3</sub>	5( $\pm 3$ )	0.4 <sup>0.6</sup> <sub>0.3</sub>	0.6( $\pm 0.3$ )
$\Sigma 10\text{vFUVnoSN}\dagger$	86 <sup>86</sup> <sub>86</sub>	86( $\pm 0.0$ )	0.0 <sup>0.0</sup> <sub>0.0</sub>	0.0( $\pm 0.0$ )	10 <sup>10</sup> <sub>10</sub>	( $\pm 1$ )	4 <sup>4</sup> <sub>4</sub>	4( $\pm 1$ )

strength of the ISRF,  $G_{\text{eff}}$ , is related to the amount of extinction,  $G_{\text{eff}} \propto \exp(-2.5 A_V)$ .

Our fiducial choice for the maximum distance for which we calculate 3D-averaged column densities and the ISRF field is  $d = 50$  pc. This value is motivated by the approximate average distance of O- and B-type stellar associations in the local ISM. This model limitation is appropriate for radiation propagation within the ISM midplane. However, it implies less accuracy for the ISRF along the vertical direction. Consequently, gas located more than 50 pc above or below the star-forming disc is always exposed to a maximum ISRF strength of  $G_{\text{bg}} = 0.0948$ . Nonetheless, as discussed in Sect. 2.2, this maximum distance of  $d = 50$  pc is reasonable for gas experiencing attenuation from star clusters with maximum masses present in our models.

We explore the validity of the assumption of the average distance of O- and B-type stellar associations by examining the average shortest separation between star clusters,  $d_{\star}$ , for the static  $G_0$  models (Fig. B1). We plot  $d_{\star}$  as a function of  $t - t_{\text{SFR}}$  with a  $1\sigma$  scatter as a shaded area. We also over plot the respective  $\Sigma_{\text{SFR}}$  in grey with the corresponding y-axis on the right-hand side. The average shortest separation between star clusters is weakly anti-correlated with  $\Sigma_{\text{SFR}}$ , with a Pearson correlation coefficient of  $\rho = -0.38 \pm 0.18$ , averaged over the four simulations with varying initial  $\Sigma_{\text{gas}}$ . The weighted average separation is  $\overline{d_{\star}} = 64 \pm 10$  pc. Our fiducial parameter  $d = 50$  pc is smaller than the average separation between star cluster sink

particles. This choice of  $d$  is sensible, as we aim to prevent the local attenuation of a cell from being influenced by multiple nearby star clusters. The rationale is to avoid accounting for sightlines that pass through other star clusters, given that star cluster sink particles are treated as point sources. It's important to note that the local column densities shielding each cell are calculated as 3D averages along multiple lines of sight to the cell.

We test the impact of different maximum FUV propagation distances,  $d$ , on  $\Sigma_{\text{SFR}}$  by running two additional models similar to  $\Sigma 10\text{vFUV}$ , but with  $d = 100$  pc and  $d = 250$  pc, respectively. A radial distance of  $d = 250$  pc is the longest realisable distance in our periodic simulation domain with a side length of  $L_x = L_y = 500$  pc. The results of the  $\Sigma_{\text{SFR}}$  test are presented in Fig. B2. Please note the linear scale on the ordinate. We simulate and show the behaviour at the start of star formation and around the first peak of star formation. The total integrated stellar mass in those time bins is  $M_{\star} = [1.81, 1.69, 1.76] \times 10^4 M_{\odot}$ , respectively. The total stellar mass shows no monotonic trend with varying distances. We conclude that the free model parameter  $d$  affects the SFR only minimally, and our fiducial choice of  $d = 50$  pc is adequate for all simulations.

The choice of parameter  $d$  influences both the 3D averaged  $A_{V,3D}$  and the extent of FUV radiation exposure in the computational domain. A larger  $d$  results in higher  $A_{V,3D}$  values due to integration over extended sightlines, while simultaneously increasing the number of cells exposed to FUV radiation from each cluster. We investigate the

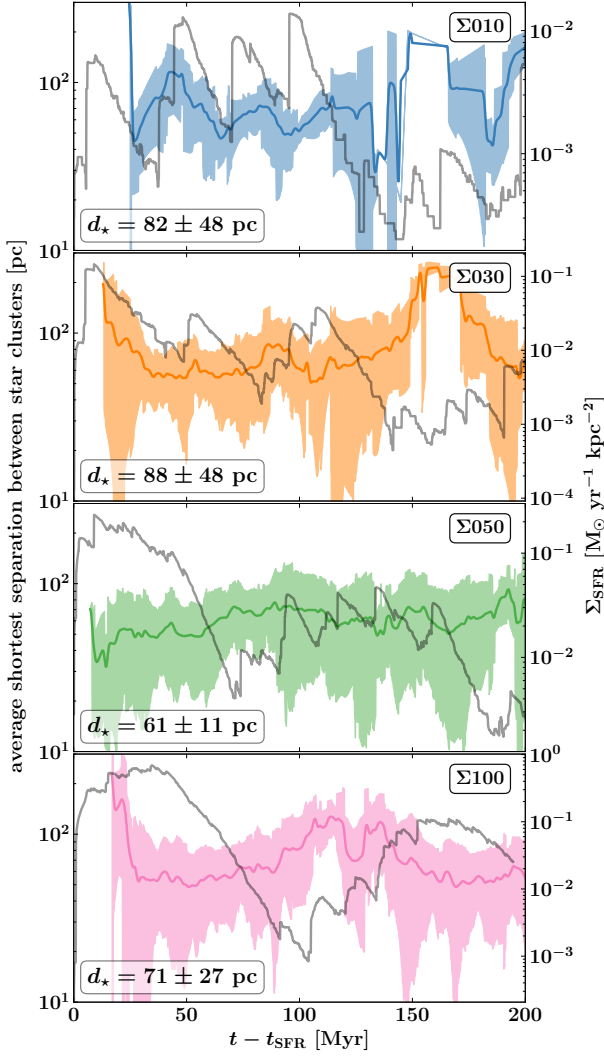


**Figure B1.** Average shortest separation between two star clusters,  $d_*$ , as a function of time. The colour-coded solid lines show  $d_*$  with  $1\sigma$  scatter as the shaded area. We quote the global average shortest separation between two star clusters with  $1\sigma$  uncertainty in the top-right boxes of each panel. For reference, we indicate  $\Sigma_{\text{SFR}}$  as a grey line (right-hand y-axis).

effect of varying  $d$  on the FUV ISRF distribution in Fig. B3. This analysis involves rerunning the  $\Sigma 010v\text{FUV}$  simulation at peak star formation with different  $d$  values, following a similar approach to that used in Fig. 14 and 15. Our results show that the ADAPTIVEG0 models with different FUV propagation distances exhibit similar behaviour at the high end of the FUV ISRF distribution, corresponding to regions in close proximity to star clusters. In the  $D050$  and  $D100$  models, the majority of gas cells experience an effective FUV field strength of  $G_{\text{eff}} = G_{\text{bg}}$ . However, the  $D250$  model displays a bimodal  $G_{\text{eff}}$  distribution, with peaks at  $G_{\text{eff}} = 4.8$  and  $G_{\text{eff}} = G_{\text{bg}}$ . The primary distinction between the  $G_{\text{eff}}$  distributions in the  $D050/D100$  models and the  $D250$  model lies in the cells located farther from the star-forming midplane ISM.

The impact of varying  $d$  is also evident in the  $\Gamma_{\text{PE}}$  distribution, as shown in Fig. B4. The  $D050$  and  $D100$  realisations (represented by blue and orange lines, respectively) exhibit similar distributions, with overlapping characteristic peaks at low to intermediate heating rates. Extending the FUV propagation to 100 pc results in a  $\sim 0.5$  dex

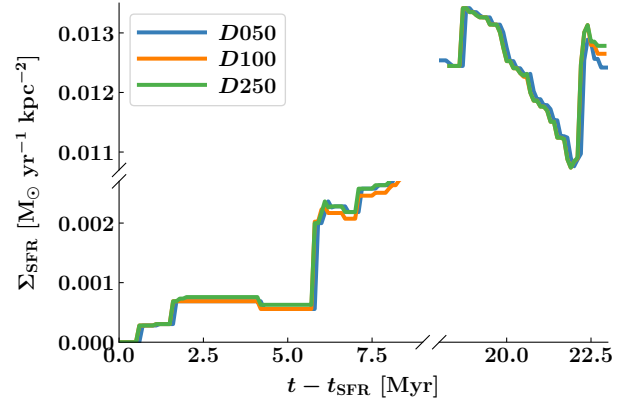


**Figure B2.**  $\Sigma_{\text{SFR}}$  for varying maximum distance of the FUV field calculation,  $d$ , ranges between the fiducial 50 pc ( $D050$ , identical to  $\Sigma 010v\text{FUV}$ ) to 250 pc ( $D250$ , the maximum possible distance given the geometry of our setup). All models are based on  $\Sigma 010v\text{FUV}$ . The free parameter  $d$  affects  $\Sigma_{\text{SFR}}$  only minimally, at most.

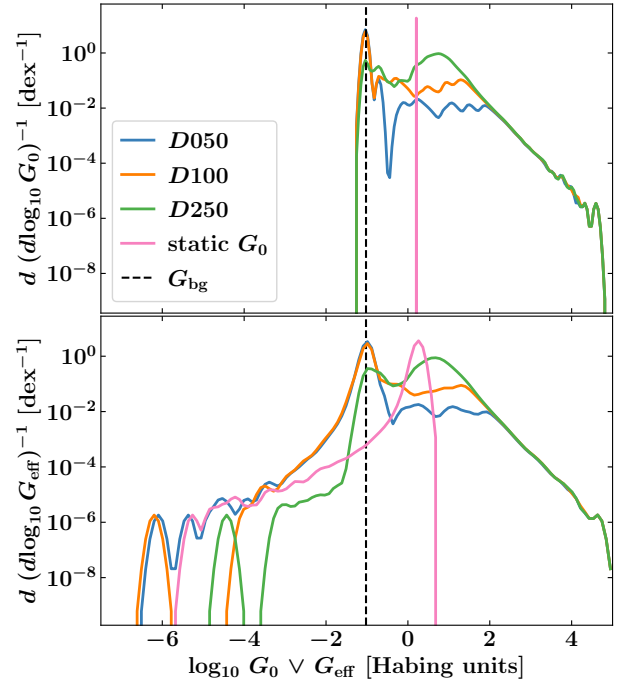


**Figure B3.** Distribution of  $G_0$  (top) and  $G_{\text{eff}}$  (bot) for one snapshot of the  $\Sigma 010v\text{FUV}$  simulation with varying maximum FUV propagation distance,  $d$ . The high-end of the distribution (i.e. regions close to star clusters) is identical for ADAPTIVEG0 models.

higher probability density at moderate  $\Gamma_{\text{PE}} \approx 10^{-25} \text{ erg s}^{-1} \text{ cm}^{-3}$ . However, this leads to only a marginal difference in the cumulative VFF of  $\Gamma_{\text{PE}}$ , as depicted in the bottom panel of Fig. B4. The heating rate to which 95 per cent of the volume is exposed differs by  $\sim 0.3$  dex between  $D050$  and  $D100$ , and by 0.6 dex when compared to the static  $G_0$  model. The situation is qualitatively different for the  $D250$  test model. The  $\Gamma_{\text{PE}}$  to which 95 per cent of the volume is exposed is a full order of magnitude higher in  $D250$  compared to the static  $G_0$  model and  $\sim 1.5$  dex higher compared to  $D050$  and  $D100$ . It's important to note that while this leads to enhanced heating rates, massive star formation remains largely unaffected due to the

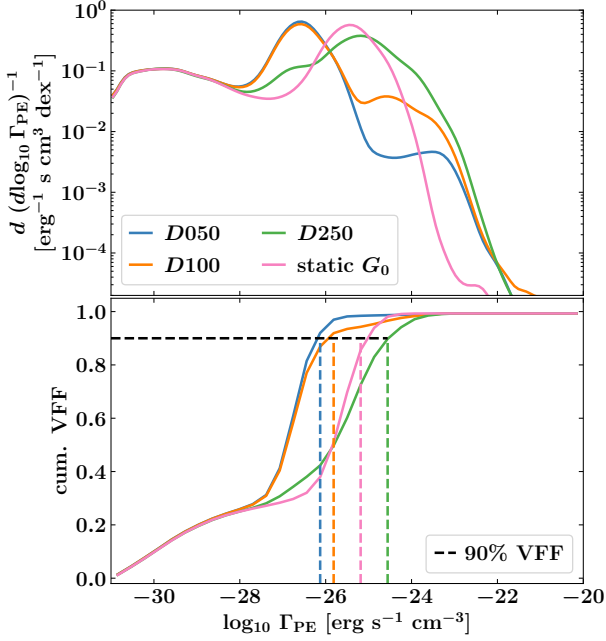


**Figure B4.** Distribution of  $\Gamma_{\text{PE}}$  for the test models with different  $d$ , similar to Fig. 14 and Fig. 15.

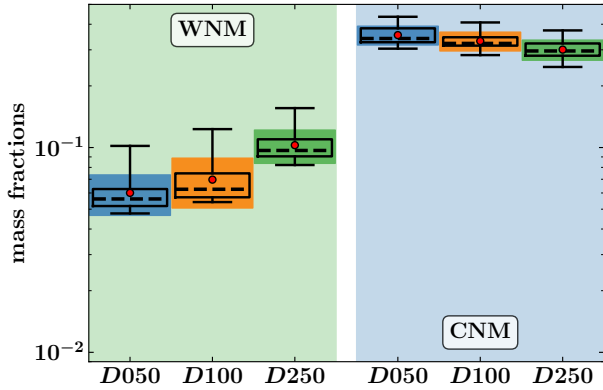


**Figure B5.** WNM and CNM MF for different values of  $d$  measured in a  $\sim 5$  Myr window around the peak of star formation. The plot has the same layout as Fig. 17. The models  $D050$  and  $D100$  are in reasonable agreement with each other. Especially for the WNM MF,  $D250$  breaks out of this agreement. The slight increase in the WNM can be explained by increased  $\Gamma_{\text{PE}}$  VFF.

dominance of HII region-generating EUV radiation and stellar winds in the immediate vicinity of young massive stars.

Our current model for the FUV ISRF is limited to accessing the 3D-averaged visual extinction calculated for each gas cell at each timestep. The computation of the local column densities and hence the visual extinction needs a reasonably small value of  $d$  to capture only the local gas structure instead of averaging out the properties of the midplane ISM. Averaging the column density over radial lines of sight with a 250 pc length (i.e. half the size of our computational domain in the horizontal plane) will result in a single plane-averaged visual extinction in the midplane ISM. Local gas and dust structures would be fully ignored and averaged out over in the midplane ISM.

Similar to Fig. 17, we show the WNM and CNM MF of the  $D050$ ,  $D100$ , and  $D250$  test models around the peak of star formation in

Fig. B5. The averaged ( $\pm 1\sigma$ ) values of the WNM MF are  $6(\pm 1)$ ,  $7(\pm 2)$ , and  $10(\pm 2)$  per cent, respectively. For the CNM MF, we find  $35(\pm 4)$ ,  $33(\pm 3)$ , and  $30(\pm 3)$  per cent during that 5 Myr period around peak star formation. The CNM MF only decreases slightly between the fiducial model  $D050$  and  $D250$ , while the impact on the WNM mass fraction is more pronounced.

Combining the above tests demonstrates a reasonable choice for  $d$  should be below 100 pc. In the context of massive star formation, the free parameter  $d$  choice does not influence the outcome, as expected from theoretical considerations. The heating rates and gas phase structure near star cluster sink particles do not experience any change with a change in  $d$ . For regions further away from active star clusters, the choice of  $d$  has an impact and must be chosen reasonably. In our current model limitations of the 3D averaged column density calculations, a sensible choice, based on the average separation of star clusters (see Fig. B1), is  $d = 50$  pc. Increasing  $d$  to scales larger than 100 pc leads to problems with the consistent computation of local visual extinctions and column densities, based on the TREERAY/OPTICALDEPTH algorithm.

## APPENDIX C: HOW DOES THE FAR-ULTRAVIOLET INTERSTELLAR RADIATION FIELD AFFECT THE CHEMISTRY?

We list all processes in which the FUV ISRF directly affects our chemical network, which is based on Nelson & Langer (1997) and Glover & Mac Low (2007). In addition to changing the chemical composition of the gas, we also account for the changes in thermal energy due to the chemical processes (see Glover & Mac Low 2007, for details).

### Photoelectric heating

(based on Bakes & Tielens 1994; Bergin et al. 2004)

$$\Gamma_{\text{PE}} = 1.3 \times 10^{-24} \cdot \epsilon \cdot G_{\text{eff}} \cdot n_{\text{H,tot}} \quad (\text{C1})$$

$$\epsilon = 0.049 \cdot \left(1 + (\Psi/963)^{0.73}\right)^{-1} + \left(0.037 \cdot (T/10^4)^{0.7}\right) \cdot \left(1 + 4 \times 10^{-4} \cdot \Psi\right) \quad (\text{C2})$$

$$\Psi = G_{\text{eff}} \cdot \sqrt{T} \cdot n_e^{-1}, \quad (\text{C3})$$

with the PE heating efficiency,  $\epsilon$  (Wolfire et al. 2003), electron number density,  $n_e$ , and total hydrogen number density,  $n_{\text{H,tot}}$ .

### Photodissociation of $\text{H}_2$

$$R_{\text{pd}, \text{H}_2} = R_{\text{pd}, \text{H}_2 \text{ thin}} f_{\text{dust}, \text{H}_2} f_{\text{shield}, \text{H}_2}, \quad (\text{C4})$$

$$R_{\text{pd}, \text{H}_2 \text{ thin}} = 3.34 \times 10^{-11} G_0 \text{ s}^{-1}, \quad (\text{C5})$$

with the  $\text{H}_2$ -photodissociation rate in optically thin gas,  $R_{\text{pd}, \text{H}_2 \text{ thin}}$  (Heays et al. 2017), the dust shielding of  $\text{H}_2$  factor,  $f_{\text{dust}, \text{H}_2} = \exp(-3.5 A_V)$  with visual extinction,  $A_{V,3D}$ , and the  $\text{H}_2$  self-shielding factor,  $f_{\text{shield}, \text{H}_2}$  provided by Draine & Bertoldi (1996).

### Photodissociation of CO

$$R_{\text{pd}, \text{CO}} = R_{\text{pd}, \text{CO thin}} f_{\text{dust}, \text{CO}} f_{\text{shield}, \text{CO}}, \quad (\text{C6})$$

$$R_{\text{pd}, \text{CO thin}} = 1.43 \times 10^{-10} (G_0/1.7) \text{ s}^{-1}, \quad (\text{C7})$$

with the CO-photodissociation rate in optically thin gas,  $R_{\text{pd}, \text{CO thin}}$  (Heays et al. 2017), the dust shielding of CO factor,  $f_{\text{dust}, \text{CO}} =$

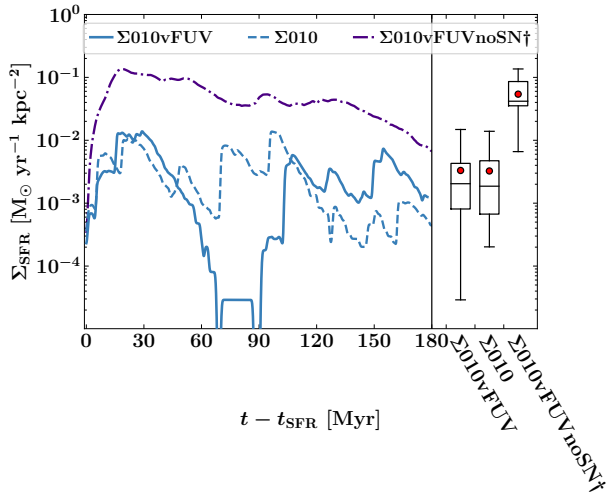


**Figure D1.** Long-term evolution of  $\Sigma_{\text{SFR}}$  as a function of simulated time after the onset of star formation,  $t - t_{\text{SFR}}$  for the solar neighbourhood models,  $\Sigma010\text{vFUV}$ ,  $\Sigma010$  and  $\Sigma010\text{vFUVnoSN}\dagger$ . We also include the box plots for the  $\Sigma_{\text{SFR}}$  distribution, similar to Fig. 10.

$\exp(-2.5 A_V)$  (van Dishoeck & Black 1988), with visual extinction,  $A_{V,3D}$ , and the CO self-shielding factor,  $f_{\text{shield,CO}}$  provided by Lee et al. (1996).

In the chemical network based on Nelson & Langer (1997), it is assumed that any carbon not bound in CO exists as  $\text{C}^+$ , due to carbon’s low ionisation potential of  $\sim 11.3$  eV. This assumption is reasonable for static  $G_0$  implementations. However, in `ADAPTIVEG0` models where much of the ISM experiences a weaker ISRF,  $\text{C}^+$  might potentially recombine into atomic C. We do not expect this potential inaccuracy to significantly affect our results regarding molecular hydrogen gas or star formation properties. As discussed in Rathjen et al. (2021), the CO abundance in our simulation framework is likely underresolved at our maximum spatial resolution of  $dx \approx 3.9$  pc. Consequently, we refrain from making claims about CO abundance or its influence on our models’ chemical dynamics.

#### Dust temperature, $T_{\text{dust}}$

We model the equilibrium dust temperature  $T_{\text{dust}}$  by balancing the ISRF heating and collisions with the gas with the thermal emission of the dust (Glover et al. 2010; Glover & Clark 2012),

$$\Gamma_{\text{ISRF}} - \Lambda_{\text{dust}} + \Gamma_{\text{gd}} + \Gamma_{\text{H}_2} = 0, \quad (\text{C8})$$

$$\Gamma_{\text{ISRF}} = \exp(-2.5 A_V) \Gamma_{\text{thin}}, \quad (\text{C9})$$

$$\Gamma_{\text{thin}} = 5.6 \times 10^{-24} n_{\text{H,tot}} (G_0/1.7) \text{ ergs}^{-1} \text{ cm}^{-3} \quad (\text{C10})$$

with the dust heating rate through absorption of FUV photons,  $\Gamma_{\text{ISRF}}$ , the optically thin dust heating rate,  $\Gamma_{\text{thin}}$  (Goldsmith 2001), the dust radiative cooling rate,  $\Lambda_{\text{dust}}$ , the energy transfer rate through collisions from gas to dust,  $\Gamma_{\text{gd}}$ , and the dust heating rate through  $\text{H}_2$  formation on dust grains,  $\Gamma_{\text{H}_2}$ .

## APPENDIX D: STAR FORMATION RATE LONG-TERM EVOLUTION

We show the long-term evolution of  $\Sigma_{\text{SFR}}$  in the solar neighbourhood models  $\Sigma010\text{vFUV}$  and  $\Sigma010$ , as well as  $\Sigma010\text{vFUVnoSN}\dagger$  in Fig. D1. We further evolve only those models with a lower initial  $\Sigma_{\text{gas}}$ , balancing computational costs against necessity. As shown in

**Table D1.** Star formation rate surface density,  $\Sigma_{\text{SFR}}$ , in our  $\Sigma010\text{vFUV}$  and  $\Sigma010$  runs. The data is calculated for a time range of  $t - t_{\text{SFR}} = [10, 180]$  Myr. We discard the first 10 Myr after the onset of star formation to reduce the artificial impact due to the initial conditions of the simulations. We quote the median value in the first data column with the 75<sup>th</sup> percentile and 25<sup>th</sup> percentile as upper and lower bounds. In the second and third data columns, we quote the time-averaged mean and the standard deviation of the mean, respectively. All values are given in units  $10^{-3} M_{\odot} \text{ yr}^{-1} \text{ kpc}^{-2}$ .

	median	mean	$1\sigma$
	[ $\times 10^{-3} M_{\odot} \text{ yr}^{-1} \text{ kpc}^{-2}$ ]		
$\Sigma010\text{vFUV}$	$1.9^{4.2}_{0.3}$	3.2	3.6
$\Sigma010$	$1.9^{5.7}_{0.7}$	3.3	3.4

Sect. 3.1, the self-consistent treatment of the FUV ISRF generated by stellar clusters has a negligible impact on  $\Sigma_{\text{SFR}}$ . We detect an unexpectedly strong dip in  $\Sigma_{\text{SFR}}$  for  $\Sigma010\text{vFUV}$  during the time-frame  $t - t_{\text{SFR}} = [67.4 : 92.4]$  Myr. However, this decrease in  $\Sigma_{\text{SFR}}$  does not stem from self-regulation through stellar feedback but from large-scale gas dynamical effects. A rather weak galactic outflow establishes itself before the quiescence phase, partially depleting the star-forming gas reservoir. This extinguishes further star formation, which in hand allows the gas to fall back and accumulate onto the midplane ISM<sup>7</sup>. We would expect that the infall and accumulation of gas onto the midplane ISM would increase the gas density and trigger star formation events.

However, our subgrid sink particle star cluster formation prescription has a set of checks in place before star cluster particles can be formed to ensure the physical plausibility of the method. We require the gas to be above a threshold density of  $\rho_{\text{thr}} = 2 \times 10^{-21} \text{ g cm}^{-3}$ . Also, we do not form new sink particles within 6 cells of an existing sink particle due to numerical stability (*overlap criterion*). We further demand (i) that the gas in the surrounding cells is in a converging flow ( $v_{\text{rad}} \leq 10^{-5} c_s$ , with the radial gas velocity,  $v_{\text{rad}}$ , and the local sound speed of the cell,  $c_s$ , *converging flow criterion*); (ii) that the gas sits in a gravitational potential minimum (*potential criterion*); (iii) that the gas is Jeans unstable (*Jeans criterion*).

During the quiescent phase, while gas is accumulating in the midplane ISM, we indeed observe simulation cells with overall densities getting as high as  $\rho \sim 10 \times \rho_{\text{thr}}$  but the additional checks prevent the formation of more star cluster particles. We check for the star cluster sink particle formation and accretion conditions at every hydrodynamical timestep,  $dt$ , for each cell in the domain. During the 25 Myr ( $t - t_{\text{SFR}} = [67.4, 92.4]$  Myr), the simulation evaluated a total of 6090  $dt$  and prevented sink particle formation a total of  $\sim 14800$  times. That is on average  $\sim 2.4$  prohibited sink particles per hydrodynamical timestep. Out of those,  $\sim 88$  per cent have been prohibited due to the overlap criterion, another  $\sim 10$  per cent due to the potential criterion and finally  $\sim 3$  per cent due to the converging flow criterion. Please note that no further checks are made once one prohibiting criterion is triggered. This means that even though  $\sim 88$  per cent of the preventive checks are due to the overlap criterion, the parcel of gas in question could also have been Jeans stable, in a diverging flow or outside a gravitational potential minimum. This behaviour is indeed to some extent peculiar and not very common. However, we want to stress that it is not nonphysical and fully results from the overall

<sup>7</sup> See Rathjen et al. (2023) for more discussion about the cyclical nature of the SFR governed by galactic outflow and subsequent inflow and the dynamical impact of CNMs in launching and supporting galactic outflows.



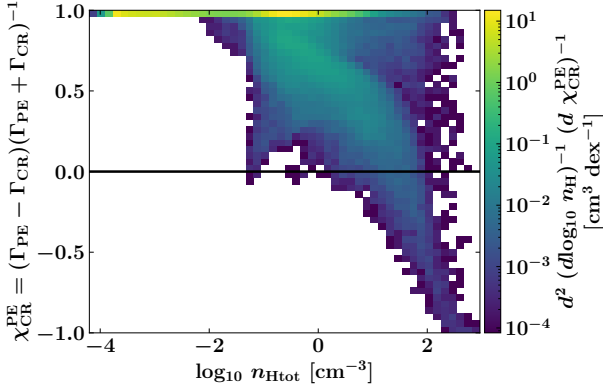


**Figure E1.** Joint PDF of the relative strength of the CR and PE heating mechanisms,  $\chi_{\text{CR}}^{\text{PE}}$ , and the total hydrogen number density,  $n_{\text{Htot}}$  of the same model and snapshot as in the heating rate analysis in Sect. 3.3. PE heating is the dominant heating mechanism of the two.

gas dynamics in the simulation during this period. The physical reasoning behind preventing sink particles from forming within another sink particle’s accretion radius is the idea that the gas within a sink particle’s radius is dynamically heated by interacting with the stars. When a parcel of gas is in conditions that it would be star-forming but it is also in the vicinity of another sink particle we let the gas be accreted onto that existing sink particle instead.

Moreover, as soon as the dynamical state of the gas is again favourable for star cluster sink particle formation,  $\Sigma_{\text{SFR}}$  picks up again and levels in at the same magnitude as  $\Sigma_{\text{SFR}}$  in  $\Sigma 010$ , indicating again the process of self-regulation through primarily hydrogen-ionising radiation, as well as stellar winds and SNe. An animation<sup>8</sup> of the overall evolution of the simulation illustrates this explanation further. We quote the averaged  $\Sigma_{\text{SFR}}$  for the long-term evolution runs in Table D1.

#### APPENDIX E: COSMIC RAY IONISATION HEATING VS. PHOTOELECTRIC HEATING

Another important heating mechanism in the ISM is the ionisation of molecular and atomic hydrogen through CRs. Assuming each ionisation process deposits 20 eV of heat energy in to the ISM (Goldsmith & Langer 1978), we compute the CR heating rate as

$$\Gamma_{\text{CR}} = 3.2 \times 10^{-11} \zeta_{\text{CR}} (n_{\text{H}} + n_{\text{H}_2}) [\text{ergs}^{-1} \text{cm}^{-3}], \quad (\text{E1})$$

with the CR ionisation rate,  $\zeta_{\text{CR}}$ . The value of  $\zeta_{\text{CR}}$  scales with the initial  $\Sigma_{\text{gas}}$  of each simulation between  $\zeta_{\text{CR}} = [3 \times 10^{-17} : 3 \times 10^{-16}]$ .

We introduce the relative strength of  $\Gamma_{\text{CR}}$  compared to  $\Gamma_{\text{CR}}$  as  $\chi_{\text{CR}}^{\text{PE}} = (\Gamma_{\text{PE}} - \Gamma_{\text{CR}})/(\Gamma_{\text{PE}} + \Gamma_{\text{CR}})^{-1}$  and show the joint PDF of  $\chi_{\text{CR}}^{\text{PE}}$  and  $n_{\text{Htot}}$  in Fig. E1. A value of  $\chi_{\text{CR}}^{\text{PE}} = 1$  indicates that no CR ionisation heating is present (e.g. in an already fully ionised region) while a value of  $\chi_{\text{CR}}^{\text{PE}} = -1$  would indicate a region fully shielded from the FUV ISRF and only penetrable by CRs. We therefore see a moderate anti-correlation of  $\chi_{\text{CR}}^{\text{PE}}$  and  $n_{\text{Htot}}$  with a Pearson correlation coefficient of  $\rho = -0.42$ . However, most of the midplane gas, 88 per cent by mass and 98 per cent by volume, is exposed to stronger  $\Gamma_{\text{PE}}$  than  $\Gamma_{\text{CR}}$ .

We want to note that in this iteration of the SILCC PROJECT,  $\zeta_{\text{CR}}$

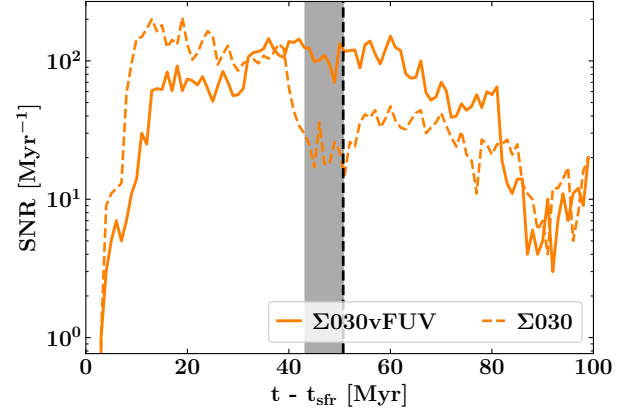


**Figure F1.** SNe rate (SNR) for the models with initial  $\Sigma_{\text{gas}} = 30 M_{\odot} \text{pc}^{-2}$ . The grey shaded area indicates the period in which the WIM MF in  $\Sigma 030\text{vFUV}$  peaks.

is to be assumed constant throughout an individual simulation and it does not scale with local gas properties or CR energy densities. A more detailed analysis of the impact of CR ionisation heating and its interplay with PE heating carried out with an updated and more self-consistent model for the CR ionisation heating will be presented in Brugaletta et al. (*in prep.*)

#### APPENDIX F: THE PEAKS IN THE WARM IONISED MEDIUM MASS FRACTIONS

In Sect. 3.4 Fig. 18, we see two outlier peaks in the WIM MF and corresponding troughs in the CNM MF, once in  $\Sigma 010\text{vFUV}$ , and once in  $\Sigma 030\text{vFUV}$ . Those outliers can also be seen in the MF distribution in Fig. 17. FUV radiation is not able to photoionise the gas and can hence be excluded as the direct source of this momentary increase in warm ionised gas. We explore whether secondary effects of the self-consistent FUV treatment or other factors are responsible for the observed MFs. We focus on the run  $\Sigma 030\text{vFUV}$  but our conclusions are transferable to  $\Sigma 010\text{vFUV}$ .

The WIM MF of  $\Sigma 030\text{vFUV}$  peaks at  $t - t_{\text{SFR}} \approx 49.2$  Myr and starts to build-up during the preceding  $\sim 7.5$  Myr. As seen in Fig. 9,  $\Sigma_{\text{SFR}}$  slightly increases during that period by a factor of  $\sim 2$ . That increase in magnitude of  $\Sigma_{\text{SFR}}$  alone is not sufficient to explain the peak in the WIM MF, as similar behaviour in  $\Sigma_{\text{SFR}}$  seen in all simulations does not lead to outliers of that extent. However,  $\Sigma_{\text{SFR}}$  only measures the total mass transformed into stars, which tells only half the truth. It is not only important to know how many stars are formed but also with what masses. The relative impact of stellar feedback of 10 stars with  $M_{\star} = 10 M_{\odot}$  is lesser than the impact of stellar feedback of a single  $M_{\star} = 100 M_{\odot}$  star (see e.g. Fig. 1). In our star formation model, stars are formed stochastically by sampling from a given IMF, whenever enough gas mass is accreted. We use the same random seed for each simulation but the spatial and temporal distribution of star formation changes of course between our simulations. This leads to a non-predictable variation of the stellar mass distribution in models with varying gas dynamics and initial conditions. But not only the masses of the individual stars are important but also their clustering. A star embedded in a dense environment has its feedback efficiency greatly reduced through radiative losses. When multiple stars exist clustered in space and time, their feedback efficiency is boosted and the feedback can penetrate deeper into the

<sup>8</sup> Which will be hosted at the SILCC PROJECT website (<https://hera.ph1.uni-koeln.de/~silcc/>).

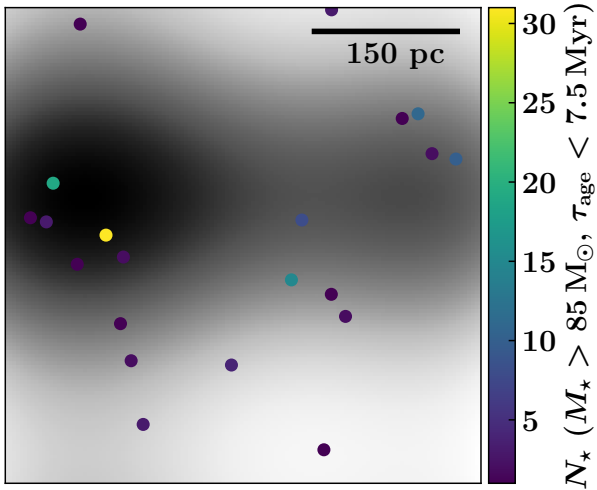


**Figure F2.** Spatial distribution in the  $x - y$ -plane (i.e. disc seen face-on) of star cluster sink particles which host super-massive ( $M_\star > 85 M_\odot$ ) and young ( $\tau_{\text{age}} < 7.5 \text{ Myr}$ ) stars. The colour bar encodes the number of those stars,  $N_\star$ . A slice through the midplane ( $z = 0 \text{ pc}$ ) of a 3D Gaussian kernel density estimate of the  $N_\star$ -weighted spatial distribution is shown in greyscale.

surrounding ISM (see e.g. Rathjen et al. 2021; Smith et al. 2021; Andersson et al. 2024). First, we can inspect the supernova rate (SNR) over time of  $\Sigma 030\text{vFUV}$  and  $\Sigma 030$  in Fig. F1. We indicate the time of the WIM MF peak with a vertical dashed line and the build-up period before as a grey-shaded area. The average SNRs prior the WIM peak period are  $\text{SNR} = 93 \pm 31 \text{ Myr}^{-1}$  and  $\text{SNR} = 111 \pm 35 \text{ Myr}^{-1}$  for  $\Sigma 030\text{vFUV}$  and  $\Sigma 030$ , respectively. During the WIM peak period, the SNR in  $\Sigma 030\text{vFUV}$  reaches a quasi-steady state while the SNR in  $\Sigma 030$  drops drastically, resulting in  $\text{SNR} = 32 \pm 8 \text{ Myr}^{-1}$  and  $\text{SNR} = 95 \pm 31 \text{ Myr}^{-1}$ , respectively. This shows, that the magnitude of star formation and stellar feedback is not responsible for the peak in the WIM MF of  $\Sigma 030\text{vFUV}$ .

In Fig. F2, we show the  $x - y$ -plane spatial distribution of star cluster sink particles which host a stellar population with young ( $\tau_{\text{age}} < 7.5 \text{ Myr}$ ) and super-massive ( $M_\star > 85 M_\odot$ ) stars existing at  $t - t_{\text{SFR}} \approx 49.2 \text{ Myr}$  in  $\Sigma 030\text{vFUV}$ , colour-coded by the number of those stars,  $N_\star$ , in each cluster. It is evident, that star formation during this period is highly clustered. We further highlight the clustering by showing a  $N_\star$ -weighted 3D Gaussian kernel density estimate slice ( $z = 0 \text{ pc}$ ) in greyscale. The amount of young, super-massive stars within a small region ( $L < 150 \text{ pc}$ ) exceeds the total number of similar stars outside this region. This strong clustering of massive stars leads to highly efficient photoionisation and stellar wind feedback, which is responsible for the temporary increase in the WIM MF. Those very massive stars, however, only live for a short time before they explode as core-collapse SNe and the warm ionised gas of the ISM decreases again towards a quasi-equilibrium state while also replenishing the CNM.

This paper has been typeset from a  $\text{\TeX}/\text{\LaTeX}$  file prepared by the author.